Advancing Additive Nanomanufacturing of Quantum Optoelectronics

Gregory Guymon

A dissertation
submitted in partial fulfillment of the
requirements for the degree of

Doctor of Philosophy

University of Washington
2025

Supervisory Committee:
J. Devin MacKenzie, Chair
Daniel R. Gamelin
Arka Majumdar
Junlan Wang

Program Authorized to Offer Degree:
Mechanical Engineering

University of Washington

Abstract

Advancing Additive Nanomanufacturing of Quantum Optoelectronics

Gregory G. Guymon

Chair of the Supervisory Committee:
J. Devin MacKenzie
Mechanical Engineering

The fabrication of quantum optoelectronic devices faces significant challenges due to the limitations of conventional nanomanufacturing techniques, which hinder the precise integration of quantum materials with nanophotonic structures. This dissertation investigates electrohydrodynamic inkjet (EHDIJ) printing as a transformative nanomanufacturing approach that enables additive, high-resolution patterning at the nanoscale. First, EHDIJ printing is used to heterointegrate colloidal emitters onto suspended nanophotonic cavities, enhancing device performance while preserving structural integrity. Next, the technique is refined to achieve deterministic placement of single quantum dots, enabling integration into complex photonic architectures. Finally, EHDIJ printing is applied as a femtoscale reactor for synthesizing single perovskite nanocrystals with spatial and structural precision. These contributions establish EHDIJ printing as a versatile platform that unifies synthesis and integration, offering a scalable path toward sustainable manufacturing of quantum optoelectronic devices. This work opens new possibilities for quantum photonic circuits, on-chip single-photon sources, and hybrid device architectures previously limited by fabrication constraints.

Table of Contents

List of Figures

List of Abbreviations

EHDIJ	Electrohydrodynamic inkjet
QD	Quantum dot
PL	Photoluminescence
PLQY	Photoluminescence quantum yield
Q	Quality factor
AC	Alternating current
ITO	Indium tin oxide
SEM	Scanning electron microscopy
FDTD	Finite-difference time-domain
DEP	Dielectrophoresis
FWHM	Full-width half-maximum
NC	Nanocrystal
DMSO	Dimethyl sulfoxide
CHP	N-Cyclohexyl-2-pyrrolidone
SAM	Self-assembled monolayer
TEM	Transmission Electron Microscopy
AFM	Atomic force microscopy

Acknowledgements

Chapter 1, in full, is a modified reprint of the material published in Advanced Materials Technologies. Gregory G. Guymon, David Sharp, Theodore A. Cohen, Stephen L. Gibbs, Arnab Manna, Eden Tzanetopoulos, Daniel R. Gamelin, Arka Majumdar, and J. Devin MacKenzie, Advanced Materials Technologies, 2024. The dissertation author was the primary researcher and author of this paper.

Chapter 2, in full, is currently under review for publication of the material. Gregory G. Guymon, Hao Nguyen, David Sharp, Tommy Nguyen, Henry Lee, Brandi Cossairt, Arka Majumdar, Kai-Mei Fu, and J. Devin MacKenzie. The dissertation author was the primary researcher and author of this paper.

Chapter 3 contains work-in-progress material being prepared for publication. Gregory G. Guymon, Eden Tzanetopoulos, Tommy Nguyen, Daniel R. Gamelin , Kai-Mei Fu, and J. Devin MacKenzie. The dissertation author was the primary researcher and author of this work.

I would like to express my gratitude to my advisor, Prof. Devin MacKenzie, for his invaluable guidance, patience, and support throughout my doctoral studies. His mentorship helped shape my thinking and gave me the opportunity to explore and grow as a researcher. I am also thankful to my committee members for their thoughtful feedback and encouragement. I'm especially grateful to my lab mates and the WCET staff for all the rich research conversations and, perhaps even more, for the non-research ones that made this journey more enjoyable.

On a personal note, I owe my deepest thanks to my parents, Jennifer and Christopher Guymon, for their unwavering love and support throughout these years, and for teaching me the strength to persevere in the face of adversity.

Introduction

Advances in quantum optoelectronics are largely driven by two critical areas: the functionalization of photonic materials and the development of platforms to harness these materials. While there has been steady progress in both areas, the fields often remain isolated due to the significant challenge of deterministically positioning and heterointegrating materials at the nanoscale. Traditional subtractive lithography techniques that have been developed for the semiconductor industry do not lend themselves well to addressing these challenges due to material incompatibilities and low throughputs. Moreover, these techniques produce substantial material waste that is both costly and harmful to the environment. As a result, laboratory-scale techniques like drop casting and templating remain the primary methods for quantum optoelectronics research. However, these approaches force significant compromises in device functionality and architecture, driven by the limitations of the tools themselves rather than the needs of the applications.

The limitations of these traditional techniques highlight the need for new, additive nanomanufacturing methods that can precisely position and integrate quantum materials without compromising their functionality. One such emerging technique is electrohydrodynamic inkjet (EHDIJ) printing, which offers significant advantages over conventional lithography-based processes. Unlike subtractive approaches, EHDIJ printing deposits materials directly onto the substrate with nanoscale precision, enabling high-resolution patterning with greater material compatibility and without the waste associated with photolithography. Therefore, this method is uniquely suited to address the challenges of heterointegration at the quantum scale.

Building on the capabilities of EHDIJ printing, this dissertation proposes a nanomanufacturing strategy tailored for quantum optoelectronic devices. Chapter 1 will

demonstrate how EHDIJ printing can enable the use of higher performance photonic architectures that have been considered as too complex and fragile for existing heterointegration strategies. This section motivates that future devices be designed around their functional requirements, rather than being limited by the constraints of conventional manufacturing processes. Chapter 2 will describe the first novel strategy for deterministic printing of single nanoparticles, enabling them to be coupled into photonic devices that previous positioning methods were incapable of achieving. Lastly, chapter 3 will show progress in using these high-resolution printing techniques to synthesize deterministic arrays of single perovskite nanocrystals. In concert with one another, this collection of work aims to bridge the gap between material functionalization and architecture development by offering a flexible, high-precision platform for the next generation of quantum technologies.

Background

Quantum optoelectronics is an emerging field at the intersection of quantum mechanics and photonics, with applications ranging from light-emitting diodes,[1,2] photodetectors,[3–5] and photovoltaic cells[6–8] to quantum computing,[9–11] communication,[12–14] and sensing.[15,16] These devices leverage the unique properties of quantum materials, such as quantum dots (QDs), that exhibit discrete energy levels and enhanced optical behaviors when confined at the nanoscale. This phenomenon is defined as quantum confinement, which occurs when semiconductor materials are reduced to sizes smaller than their exciton Bohr radius, typically below 10 nm.[17] In this regime, the electronic and optical properties of the material are no longer governed by classical physics but by quantum mechanics. For example, in semiconductor QDs, quantum confinement allows their size to directly control their bandgap, leading to tunable emission wavelengths.[18,19] This property makes them particularly useful in applications like single-photon sources and color-accurate displays,[2,20] where precise control over light emission is crucial.

One of the most significant barriers to advancing quantum optoelectronics is the integration of quantum materials into functional devices. These materials are highly sensitive to their environment, requiring meticulous control over their placement and interaction with other components to preserve their quantum properties. A key challenge lies in deterministic positioning, the ability to place quantum materials at specific locations on a device with nanoscale precision.[9,21] Without this control, degradation of quantum behavior can occur, such as weak light-matter coupling, spectral shifting/broadening, loss of single-photon purity, reduced coherence time, and unintentional coupling with nearby components.[22]

Traditional semiconductor fabrication methods, particularly subtractive lithography, have long been the industry standard for creating micro- and nanoscale structures. These methods typically involve depositing materials onto a substrate and then etching away unwanted portions, a process that works well for large-scale semiconductor devices. However, when applied to quantum optoelectronic materials, lithography presents several limitations. First, the resolution of lithographic techniques is often insufficient to handle the precise positioning required for quantum materials, which need to be arranged with nanometer accuracy.[23] Second, many quantum materials, such as colloidal QDs, are incompatible with the high-temperature or chemical processes involved in traditional lithography, leading to material degradation.[24]

Furthermore, subtractive methods generate a significant amount of material waste. In the case of QDs, this waste not only raises production costs but also increases the environmental footprint of device fabrication.[25] This issue is particularly critical in the context of scaling quantum devices for industrial applications, where sustainable manufacturing processes are becoming increasingly important. The need for more environmentally friendly, cost-effective manufacturing is driving research into alternative techniques that can eliminate or reduce waste while maintaining high precision.

Despite these challenges, most research in quantum optoelectronics continues to rely on laboratory-scale fabrication techniques such as drop casting,[26,27] self-assembly,[28] and templating.[29,30] These methods are relatively simple and allow researchers to investigate quantum material behavior with less technical manufacturing overhead, but they offer limited control over material placement and integration. The result is often devices with compromised functionality, where the design is dictated by the limitations of the fabrication method rather than by the optimal performance of the device. For instance, drop casting can lead to non-uniform

distributions of quantum dots, and templating is often constrained by the predefined template geometry and requires excessive device contact to complete the mask. Additionally, while self-assembly can yield highly ordered nanostructures, the process is difficult to control with the precision needed for deterministic placement in optoelectronic devices. Furthermore, self-assembly often results in large-scale uniform patterns that may not align with the specific needs of a given device architecture.

To address the limitations of these traditional methods, various additive manufacturing techniques have gained attention. Inkjet printing, one of the most widely used additive methods, enables the direct deposition of nanomaterials onto substrates, making it a versatile option for various applications. However, conventional inkjet printing struggles with resolution at the quantum scale, limiting its use to devices that only require microscale (>10 μm) precision.[31–33] To achieve finer control, techniques such as direct-write and laser-assisted processes have been explored. Direct-write methods, which use fine beams for nucleation and growth of QDs, offer moderate submicron resolution but are slow and often incompatible with sensitive quantum materials.[34,35] Laser-assisted techniques, like laser-induced forward transfer which uses lasers to transfer films from a donor substrate, provide similar precision but suffer from scalability issues and limited material flexibility.[36]

Among these, electrohydrodynamic inkjet (EHDIJ) printing has emerged as a promising solution for quantum material integration. EHDIJ printing uses a high strength electric field between the printhead and the grounded substrate to create a nanoscale field focusing effect on solutions and particles, enabling the precise placement of colloidal materials. Conventionally, this is achieved through the formation of a Taylor cone, which is formed by the electrostatic potential created between the meniscus and ground plane.[37,38] Through controlled initiation and

destabilization of this Taylor cone, ordered nanostructures as low as ~35 nm in diameter have been reported.[39] This method not only offers superior resolution compared to traditional inkjet printing but also supports a wide range of materials, including those incompatible with high-temperature processes.[40] Furthermore, EHDIJ printing significantly reduces material waste, as deposition is highly localized and efficient. These advantages position EHDIJ printing as a leading technique for fabricating quantum optoelectronic devices, offering the precision and scalability necessary for next-generation technologies.

With this new strategy in mind, several critical challenges that have remained unresolved by former methods are worth looking at. One major limitation is the lack of work on complex three-dimensional integrated photonic cavities, particularly suspended cavities, which are crucial for enhancing light-matter interactions in quantum systems. These structures can improve device performance by providing better confinement of light,[41] yet current research has primarily focused on simpler, two-dimensional planar architectures, leaving a gap in the development of more advanced cavity designs.

Additionally, the field faces challenges in single particle positioning. Precise placement of individual QDs is essential for many quantum photonic applications, yet deterministic positioning techniques remain underdeveloped. Current methods, such as colloidal templating deposition or random placement, lack the compatibility or precision needed for high-performance devices.[21]

Lastly, while colloidally grown nanocrystals offer good optical properties, they suffer from agglomeration, shape/size variation, and ligand issues, standing as a gap in synthesis strategy. Moreso, it requires refined chemistry overhead to minimize inconsistencies from batch-to-batch for scalable applications and limits material usage to those that can be grown

colloidally. While there has been recent advances with high resolution templating strategies,[42] the field lacks deterministic additive nanocrystal growth techniques with highly controlled spatial and structural properties, which is critical for device scalability and integration.

The limitations of traditional fabrication methods in quantum optoelectronics, such as imprecise material placement, inefficient processes, and compatibility issues, highlight the need for innovative approaches. These methods hinder the progress of addressing the critical challenges of developing high performance device architectures, deterministically integrating singular QDs, and diversifying nanocrystal synthesis strategies. Utilizing an additive nanomanufacturing technique, EHDIJ printing, offers promising solutions by enabling contactless high resolution material positioning and enhanced scalability. This dissertation proposes leveraging this emergent technology to address the critical gaps in quantum optoelectronic research and manufacturing.

Chapter 1 Heterointegration of Quantum Dots on Suspended Nanophotonic Cavities

Background

Colloidal quantum dots (QDs) have recently been at the forefront of research in hybrid integrated large-area and photonic devices for applications ranging from consumer information displays to quantum optical devices, computing, and sensors.[13,43] Semiconductor quantum dots are of considerable interest for these applications due to their, in some cases, near-unity quantum yields, single photon emissivity, and ligand-stabilized dispersity for solution processing.[19,44–46] Furthermore, the ability to tune the emission wavelength peak of the quantum dots by adjusting their size and chemistry offers them the flexibility to couple with a broad range of photonic platforms.[47] The utility of colloidal QD emitters can be further extended via heterointegration with photonic cavities that maximize the emitter's emission intensity *via* the Purcell Effect, narrow its linewidth, and enable novel effects such as on-chip lasing and low-power optical nonlinearity.[26,48]

Silicon nitride (Si_3N_4) has emerged as one leading materials candidate for visible wavelength nanophotonic structures owing to its broad transparency window, Si CMOS compatibility, high visible refractive index, and low loss. For example, waveguides with ultralow loss and ring resonators with ultrahigh quality factors utilizing Si_3N_4 have been demonstrated.[49,50] One-dimensional photonic crystal nanobeam cavities represent an attractive geometry because their inherently small mode volumes maximize the light-matter coupling with heterointegrated QDs at visible wavelengths. However, the low refractive index of Si_3N_4 ($n \sim 2$) limits the optical band gap size and thus quality factor and mode confinement attainable in a high index local environment. To overcome these limitations and achieve higher Q-factors, researchers have

proposed suspended nanobeam cavities, as opposed to designs monolithically integrated onto the substrate.[41]

Laboratory-scale methods of integrating solution-processible QDs with these platforms have largely been confined to macroscale drop casting and spin coating, which typically deposits QDs with areal coverages with dimensions that are orders of magnitude greater than the intended target.[26,48] These processing techniques, however, have several drawbacks. First, they can result in very inefficient utilization of often toxic and environmentally concerning materials such as Cd and Pb, inconsistent with large-scale, sustainable manufacturing. Drop casting and spin coating can also lead to residual QDs outside of the intended target area that may detrimentally affect the function of other parts of the system or cause an unwanted background of emission or absorption that can mask the desired action of the device. Lastly, drop casting and spin coating techniques can put significant mechanical stresses on inherently fragile suspended nanophotonic structures due to capillary, kinetic, and thermal effects during the coating and drying stages of these processes. The materials waste and negative physical effects of these processes can be reduced by printing with conventional piezo-inkjet technology, which forms droplets >1 pL in volume and feature sizes >10 μm.[51] These dimensions, however, are still significantly larger than the often submicron feature sizes common in visible wavelength nanophotonic structures.[52] By utilizing subtractive processing, masks or templates, greater resolution and precision can be achieved, at the cost of design workarounds or concessions that must be made to accommodate the mask or template deposition and removal.

Alternatively, electrohydrodynamic inkjet (EHDIJ) printing has emerged over the past decade as an advanced manufacturing method for scalable contactless solution deposition with droplet sizes down to the attoliter scale.[53,54] EHDIJ printing is an electrophoretic additive

manufacturing process that uses an applied electric field between the nozzle and target to selectively deposit charged materials down to nanoscale resolutions (~35 nm).[39] EHDIJ printing has been investigated for manufacturing circuitry interconnects,[55–57] flexible electronics,[40,58–60] photodetectors,[61–63] solar cell electrodes,[64–66] metasurfaces,[51,67] and light emitting diodes.[68–70] In regards to EHDIJ printing nanocrystals on nanophotonic structures, early work demonstrated an electrostatic autofocusing effect that could be utilized to selectively deposit onto edge-shaped geometries (such as waveguides and pillars) with enhanced efficacy.[39,71,72] Recently, Cohen *et al*. applied these mechanisms to demonstrate EHDIJ printing of lead-halide perovskite nanocrystals onto monolithic nanophotonic cavities.[73] This work was supported with additional analysis to confirm the negligible effects of applied electric fields on the structure and performance of the QDs, thus demonstrating their strong compatibility with the EHDIJ printing process.

Herein, we address the challenges of hybrid integration for high-performance suspended nanophotonic structures through the use of contactless electrohydrodynamic inkjet printing. We utilize robust CdSe/CdS core-shell QDs as photoactive materials, prepared in a cosolvent ink designed for the EHDIJ printing process. The materials are integrated into dielectric-mode silicon nitride suspended cavity pairs, designed to photonically couple with the peak emission wavelength of the QDs, at varying cavity separation distances. This work demonstrates the first, and only known, method for deterministic positioning of quantum dots onto suspended photonic structures, with nanoscale precision.

Results and Discussion

CdSe quantum dots were synthesized via a modified hot injection colloidal synthetic approach.[74] To improve their photoluminescence quantum yield (PLQY), a CdS shell was grown over the core CdSe by slow-injection of cadmium oleate and octanethiol.[45] To prepare the synthesized core/shell QDs as a stable colloidal ink for printing, the particles were dispersed in a 1:1 octane:hexadecane mixture to a suitable concentration, indicated by the optical density of the first excitonic absorption peak (see Figure A1 in Appendices). Figure 1.1a shows the normalized absorption and photoluminescence (PL) of the stabilized colloidal QD ink, with peak PL centered about 624 nm. The inset images in Figure 1a show a colloidal QD ink under ambient light illumination (left) and UV illumination (right). The lack of sub-bandgap scattering in the absorption spectrum and the lack of haziness in the left image showcase the high colloidal stability of the QD ink. The rich, scarlet fluorescence in the right image demonstrates the strong fluorescence of the QDs in this EHDIJ ink. Figure A2 shows a TEM image of a drop cast and dried QD ink to provide a closer look at the shapes and sizes of these QDs. The QDs are spherical in shape with an average diameter of 6.1 ± 0.8 nm.

Silicon nitride nanobeams were fabricated using standard nanofabrication techniques based on Si_3N_4 thin films on Si substrates (see Experimental Methods). After lithography and etching, this process yields an array of silicon nitride nanobeams that are air-surrounded (below, to the sides, and between the waveguides), with the exception of connection of the beams to the substrate only at their fixed ends. Nanobeams were fabricated in pairs, with beam separation distances ranging from 100 nm to 500 nm. To determine the photoluminescent coupling and resonance of the QDs and the cavities, the devices were illuminated with 445 nm continuous wave excitation and measured via their PL spectrum. The observed peak of the spectrum

indicates the resonance of the cavities. The device's quality factor (Q) can be calculated according to:

$$Q = \frac{\lambda_0}{\Delta\lambda} \tag{1.1}$$

where λ_0 and $\Delta\lambda$ are the resonant wavelength and linewidth, respectively, of the cavity mode's Lorentzian line shape.

Q is a useful indicator for describing the overall spectral purity, efficiency of the emission, and coupling strength of a heterointegrated system. Higher quality factor can be associated with high spectral purity, relatively low loss, and strong light-matter coupling with emitters. Figure 1.1b shows the PL spectrum of a nanobeam with 500 nm separation distance, fit with a Lorentzian curve, revealing a quality factor of ~3400. Beams with a 500 nm separation distance can each be treated as completely isolated nanophotonic structures, demonstrated by the single sharp resonance peak at ~625 nm. However, reducing the separation distance of the beams to 100 nm yields sufficient inter-cavity electric-field overlap to enter a strongly coupled regime, as seen by the two peaks in Figure 1.1c, with Q factors of ~5400 and ~2360 for supermodes 1 and 2, respectively. This result confirms the functionality of this device's architecture for investigating the spatial influence of photonic cavities, prior to the heterointegration of photoactive materials. Inset images of Figures 1b and c highlight the cavity's suspended design, with a distinct trench etched from around and below the beams. Each device was fabricated with wedge-shaped concentric gratings to the right of the top waveguide and to the left of the bottom waveguide. These gratings diffuse light from either beam after heterointegration and indicate the presence or absence of coupling. The web-like substance below the beams is a residual byproduct of the isotropic XeF_2 etching process.

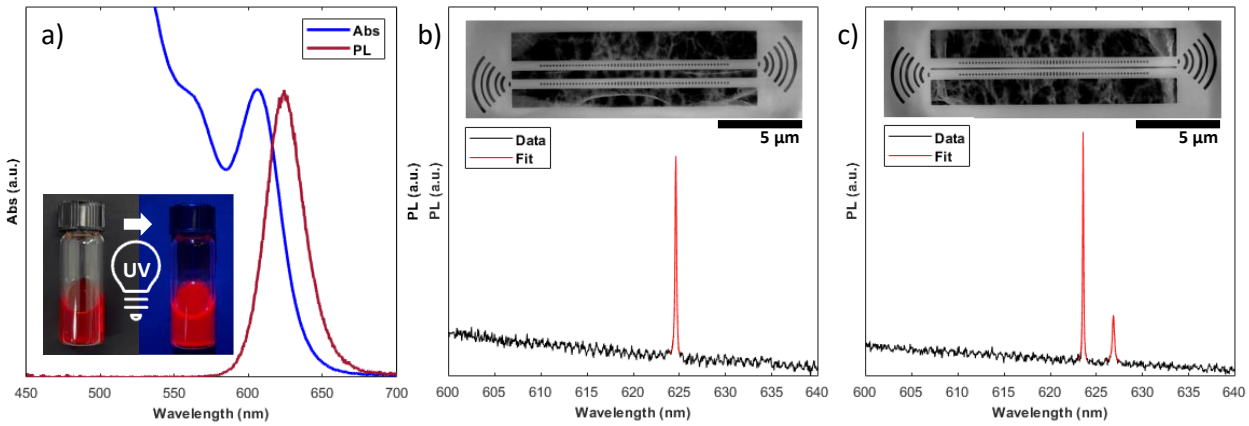

Figure 1.1. Characterization of QDs and suspended cavities. a) Normalized absorption and PL spectra of CdSe/CdS quantum dots. Inset: Image comparison of the colloidal QD ink under ambient and ultra-violet (UV) lighting conditions. b) PL characterization of 500 nm separated suspended Si_3N_4 cavity. Inset: SEM imagery of the respective fabricated device. The presence of a single mode peak at ~625 nm indicates no coupling at this distance. c) PL characterization of 100 nm separated suspended Si_3N_4 cavity. The two peaks between 620 nm and 630 are assigned to two cavity supermodes, which indicates that these cavities are strongly coupled at this distance. Inset: SEM micrographs of the respective fabricated devices.

The colloidal quantum dots were physically integrated with the nanophotonic cavities via high-resolution electrohydrodynamic inkjet (EHDIJ) printing. Figure 1.2 shows a schematic of the EHDIJ tool used for this work. Colloidal inks were pipetted into pulled borosilicate glass capillary printheads that were then magnetically mounted to an electrode on the tool. Next, the substrate containing the suspended cavity pairs were secured to a grounded printing stage via a vacuum chuck. The parameters for printing were determined by finding the minimum voltage threshold for steady-state droplet ejection on a non-etched portion of the device's substrate. The parameters were further optimized for printing on the suspended cavities by raising the minimum voltage threshold enough to prevent destabilization of the steady-state ejections, caused by the fluctuating strength of the electric field as the printhead passes over the trench of the device. The minimum voltage threshold can be raised by increasing the voltage bias above the minimum for ejection. Printing was initiated using a 75% square-wave alternating current (AC) that is activated over the pre-determined deposition sites with a bias of 230 V, an amplitude of 50 V, and

a frequency of 1 kHz. In principle, the bias polarizes the particles in the solution to overcome the surface energetics that limit droplet sizes in conventional inkjet printing and stabilizes a surface-charged convex meniscus at the tip of the printhead. The amplitude is then applied at the given frequency to overcome the surface energy of the meniscus, forming a Taylor cone that extends along the direction of the electric field. Next, hydrostatic destabilization of the tip of the Taylor cone causes droplets to form, which separate from the extended cone and are guided by the electric field towards to stage. The ejected droplet's final position is determined by the planar movement of the step-motor-driven translation stage that can move the substrate stage with 100 nm step sizes and no hysteresis. To align the printhead's deposition site to the cavity target, the printer utilizes a two-stage alignment process. The first stage determines the position and orientation of the substrate by positioning the alignment camera to calibration features on the substrate. The second stage determines the position of the printhead's nozzle by calibrating the alignment camera to an initial printing test feature. The two-stage alignment process adapts the local coordinates of the printing design by including any offset or rotation required by the position and orientation of the substrate or nozzle, relative to the stage's global coordinates. An example of the printing precision that can be achieved with this tool is demonstrated in the microscopy image of a printed CdSe/CdS QD array in Figure 1.2. Measuring the volume of as-printed QD deposits with atomic force microscopy yielded a mean of ~3.34 ± 0.86 attoliters per print (Figure A3 in Appendices). By modulating the strength of the electric field, for the micron-scale inner diameter nozzles used here, prints ranging from sub-pico to attoliter-scale volumes can be expected.

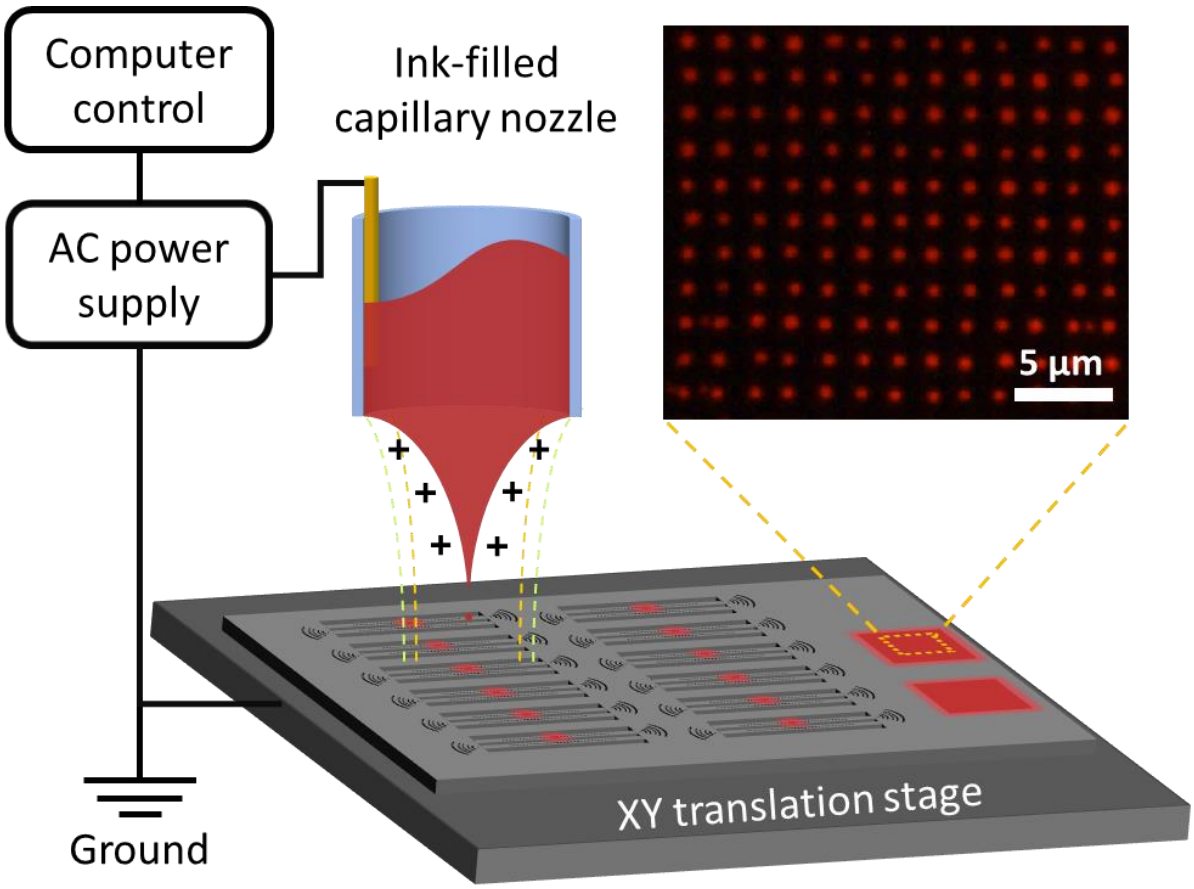

Figure 1.2. Schematic of the electrohydrodynamic inkjet printing setup. The inset image shows PL microscopy with 450 nm excitation of CdSe/CdS quantum dots printed with 2 µm pitch.

The SEM images in Figure 1.3 show a series of dielectric-mode Si_3N_4 cavities after alignment to structures on the device substrate and CdSe/CdS QD printing. Here, the presence of QDs solely on the upper beam indicates that the printed droplet only contacts and deposits QDs onto a single cavity from each pair down to cavity spacings as small as 100 nm. Close examination of the suspended cavity print sites reveal that QDs appear to be wetting the center elliptical holes, but we note a lack of QDs observable at the edge of the elliptical cavity holes near the edges of the printed QD features. This behavior is likely explained by morphologically-induced reductions in surface energy and wetting compared to unpatterned Si_3N_4, such as in Cassie-Baxter wetting states or what is sometimes referred to as “the lotus effect”, where the

surface energy cost of wetting a more complex and effectively higher surface area geometry prevents the penetration of the QD-ink.[75]

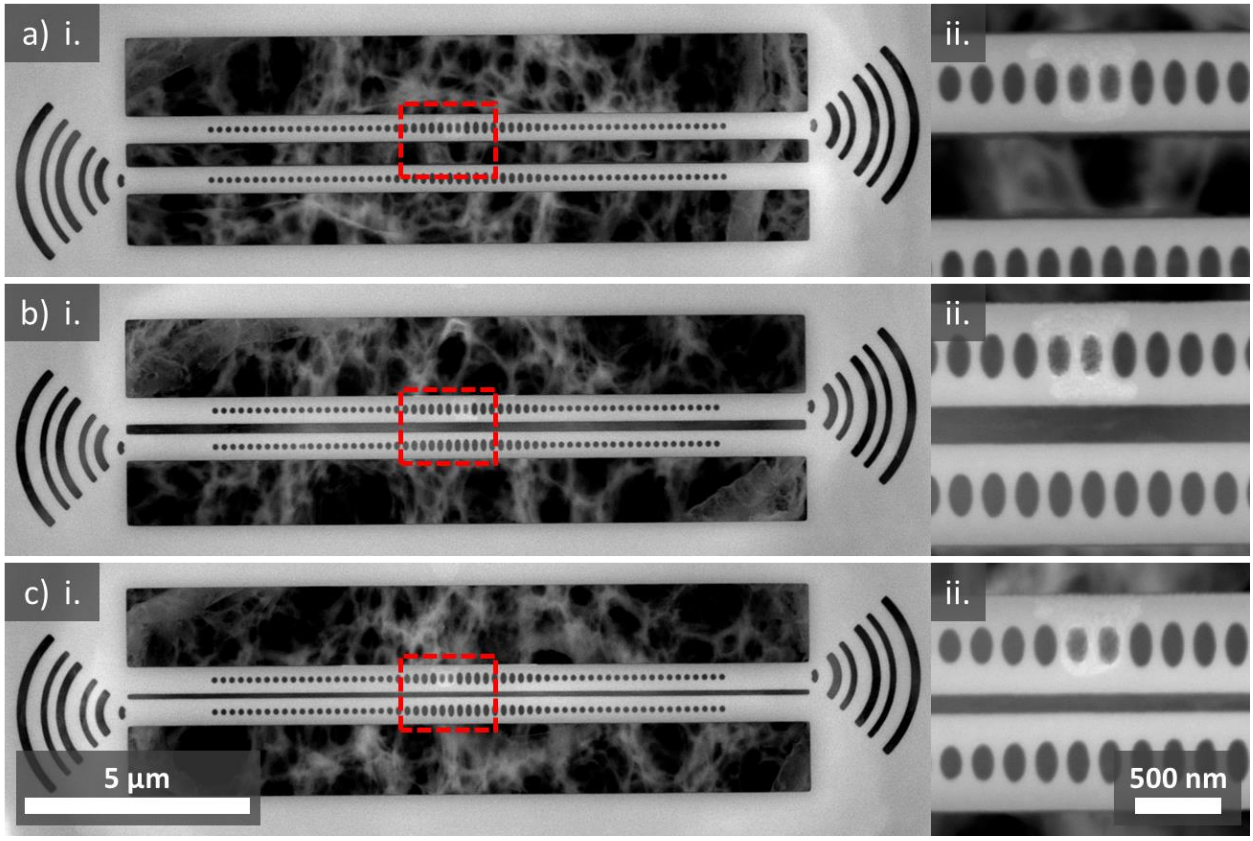

Figure 1.3. SEM imagery of suspended cavity beam pairs post-EHDIJ printing. The micrographs show an aggregation of CdSe/CdS printed on a single beam for each pair. a) 500 nm beam separation. i. Device overview image. ii. Cavity print site image. b) 200 nm beam separation. i. Device overview image. ii. Cavity print site image. c) 100 nm beam separation. i. Device overview image. ii. Cavity print site image.

Following the electrohydrodynamic inkjet printing of the QDs, the asymmetric QD-coupled nanobeam pair devices were inspected using a PL microscope under 450 nm excitation. The microscopy in Figure 1.4a-c shows suspended cavity pairs with waveguide spacings of 500, 200, and 100 nm, respectively. The emissions from the cavity and waveguide couple to the gratings at the edge of each waveguide. These gratings were used purely for qualitative microscopy measurements because their design allowed photonic coupling to be gauged by their relative brightness. In Figure 1.4a, the emissions from the right grating indicate strong coupling

between the cavity and the quantum dots. The lack of emission from the left grating indicates no inter-cavity coupling for this waveguide's separation distance. The emission visible at the top of the left grating is due to its proximity to the top waveguide, which causes minor unintended grating coupling, but does not impact the performance of the device in any meaningful way. For the 200 nm separated cavity pair (Figure 1.4b), the brightness of the right grating indicates strong coupling between the QDs and the cavity, while the brightness of the left grating indicates detectable inter-coupling. The high light intensity at both gratings (Figure 1.4c) indicates that nanobeams separated by 100 nm show the strongest inter-cavity coupling.

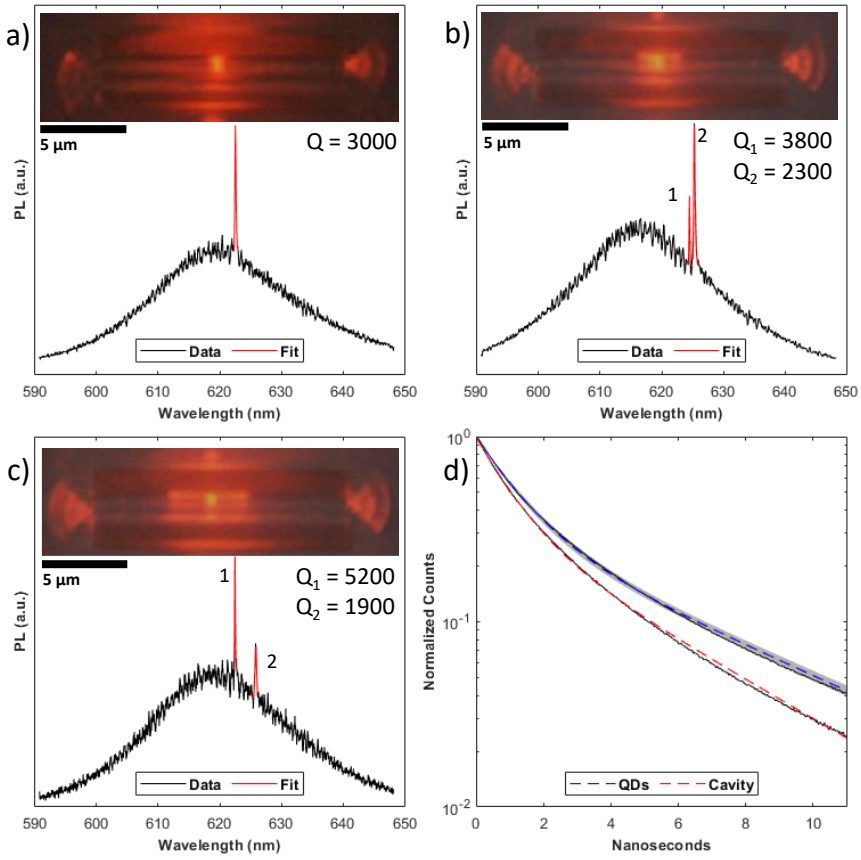

Figure 1.4. PL microscopy and characterization of QD-coupled suspended cavities. a) PL spectra of 500 nm separated suspended nanobeam cavities. Inset: PL imagery of the respective cavity. b) PL spectra of 200 nm separated suspended cavities. Inset: PL imagery of the respective cavities. c) PL spectra of 100 nm separated suspended cavity. Inset: PL imagery of the respective cavity. d) PL lifetime measurements of QDs printed on the cavity site and outside of the cavity. The QD's dashed blue line represents the best-fit biexponential to the mean of the raw data (black)

for the external QDs, accompanied by a shaded curve (gray) to represent the standard deviation of the fit. The cavity's dashed red line represents the fitted biexponential curve of the data (black) for the cavity-coupled QDs.

Having identified the photonic coupling types present and their respective strengths in each suspended cavity design through qualitative PL microscopy, we further characterized these devices through quantitative spectroscopy methods. See the Experimental Section for the methodology of the PL characterization of these devices. Figure 1.4a shows PL spectra obtained by exciting the QDs with 532 nm light and collecting the resulting cavity emission from the right end of the top grating for asymmetrically printed QD-coupled nanobeam cavities separated by 500 nm. The broad peak is assigned to non-cavity coupled emission from the QDs, and the sharp peak at ~622 nm is assigned to QD PL that is coupled to the fundamental mode of a single nanobeam cavity. We fit the sharp peak with a Lorentzian curve to obtain a quality factor of ~3000, with no other statistically significant peaks that would indicate inter-cavity coupling. As the cavity spacing is reduced to 200 nm, two sharp peaks become visible in the PL spectra shown in Figure 1.4b with a peak spacing of ~ 0.2 Å. These two peaks, or supermodes, have different quality factors ($Q_1 \approx 3800, Q_2 \approx 2300$) due to unintentional cavity fabrication variations, which leads to spectral detuning. When the supermodes are coupled, their behavior is interdependent and new eigenmodes are created that are the combination of the original modes. When these modes experience spectral detuning, meaning their respective frequencies differ slightly, their new eigenmodes differ as well. This results in offset quality factors that approximately average out to that of the isolated QD-cavity system (Figure 1.4d). In the case of these coupled supermodes, the original mode (Q_2) is slightly red-shifted while the coupled mode (Q_1) is blue-shifted in proportion to the inter-cavity spacing. To demonstrate this proportionality, Figure 1.4c shows the spectroscopy of the as-printed inter-cavity coupled device with a cavity spacing of 100

nm. Here, the separation of the supermodes ($Q_1 \approx 5200, Q_2 \approx 1900$) is increased to 3.4 nm, which corresponds to a stronger coupling strength. This behavior is in good agreement with previous work using CdSe/CdS QDs and monolithic silicon nitride nanobeam cavities.[29]

Figure 4d shows QD PL lifetime data collected from the upper cavity of Figure 4a compared to data collected for the same QDs that were printed away from the cavity. Because of the relatively large beam separation (500 nm), this system can be effectively treated as an isolated cavity for determining the Purcell enhancement of the heterointegrated device. In both cases, the PL lifetimes were fitted to a biexponential decay. For the QDs that were not coupled to any cavities, the average fast and slow PL decay was 1.18 ± 0.07 ns and 5.31 ± 0.17 ns, respectively, whereas for the cavity-coupled QDs, the fast and slow PL decay was 1.02 ns and 4.13 ns, respectively. This result corresponds to average Purcell factors of 1.15 and 1.29 for the fast and slow decay, respectively, which is in line with similar reports.[29] When compared to the maximum possible Purcell enhancement factor determined by finite-difference time-domain simulation (FDTD), the experimentally measured values were in good agreement with the simulated value of 1.34. Additional information about these calculations and data can be found in the appendices, section A1.

Colloidal quantum optical materials heterointegrated with suspended photonic devices have been explored for their potential in next-generation optical devices, but no scalable, fully additive, and sustainable method exists to deterministically place these materials on such fragile nanostructures. By successfully combining CdSe/CdS core-shell QDs with these suspended silicon nitride nanobeam cavities in this work with EHDIJ printing, we convincingly demonstrate that this printing method has great potential to help elucidate the fundamental understanding of light-matter interactions and provide a viable path to manufacture fully integrated quantum

photonic devices of unlimited scale and complexity. We show that the printing process has a minimal impact on emitter properties or cavity performance, and the patterning precision can reach length scales as small as 100 nm. To the best of our knowledge, this is the first demonstration of selective colloidal material positioning on suspended cavities at the length scales needed to demonstrate tunable inter-cavity coupling. Such fine patterning fidelity on these suspended structures could unlock the full potential of high gain nanomaterials,[76–79] magneto-optical nanoparticles,[80–82] and other narrow-linewidth emitters[30,83] with high Q-factor individual cavities,[41] cavity pairs,[84] and strain-tunable nanostructures.[85] These advanced heterointegrated systems could be used to produce PT-symmetry lasers,[86,87] fully-integrated nanoscale optical networks,[88] and other unique device architectures that could not be fabricated without the methods described here. Furthermore, previous demonstrations of single emitter positioning with EHDIJ printing[72,89] and high-yield single-particle placement of individual silica-shelled CdSe/CdS QDs[30] suggest that this printing process could enable high-yield and high-precision patterning of individual emitters on nanophotonic devices to enable the manufacturing of single photon emitter-based integrated circuits.

Furthermore, the ability to deterministically deposit colloidal QDs onto air-clad photonic structures, with nanoscale precision, has yielded immediate improvements in coupling strength when compared to previous work on polymer-clad photonic cavities, as evident from our higher Purcell enhancement.[29] This opens the gates for new hybrid integrated device architectures that were previously considered impossible from a materials integration standpoint. For instance, recent work on in-situ strain tunable suspended cavities shows the potential that EHDIJ printing could have for integrating a broad range of colloidal emitters into actively tunable photonic devices.[90]

Lastly, a significant contribution to the broad line widths of the as-printed QDs is due to the variation among emitters in an aggregate deposition. Seeking out reliable methods for deterministically positioning single QDs is becoming a focus for those interested in functionalizing colloidal emitters for their potential in single-photon manipulation and entanglement. Recent work has demonstrated the potential of giant oxide shells for singularly-positioned CdSe/CdS QDs, through capillary-driven self-assembly in substrates or removable templates.[30,91] Through ongoing optimization and reduction of QD counts, building on the work here, a path to a sustainable nanomanufacturing of single photon QD-based devices through additive heterointegration using electrohydrodynamic inkjet printing is taking shape.

Conclusion

In conclusion, we have demonstrated the first additive heterointegration method for directly patterning attoliter scale deposits of colloidal emitters selectively onto three-dimensional free-space suspended nanophotonic cavities, spaced as close as 100 nm that exhibit inter-cavity coupling. Shown through high-resolution SEM imaging, electrohydrodynamic inkjet printing was able to preserve the physical integrity of the free-space three-dimensional suspended nanobeam cavities, due to its inherently contactless process. Furthermore, PL characterization of the as-printed devices confirmed the suitability of EHDIJ printing for enabling supermode emissions from nanomanufactured QD-cavity and inter-cavity coupled nanobeams at nanoscale free-space separations. These results should encourage additional research into heterointegrated suspended devices, as further improvements to emitter quality, cavity fabrication disorder, printhead size, and stage precision would all serve to enhance overall device quality. Addressing these problems on all fronts will require convergent developments in chemistry, physics, materials science, electrical, and mechanical engineering.

Experimental Methodology

Materials

Cadmium oxide (CdO, 99.9%, Sigma Aldrich), Se powder (200 mesh, 99.99%, Alfa Aesar), 1- octadecene (ODE, 90% tech grade, Sigma Aldrich), oleic acid (OLAC, 90% tech grade, Sigma Aldrich), tri-n-octylphosphine oxide (TOPO, 99%, Sigma Aldrich), hexadecylamine (HDA, Sigma Aldrich), trioctylphosphine (TOP, 97% Sigma Aldrich), 1-octanethiol (99%, Sigma Aldrich), toluene (certified ACS, Fisher Chemical), ethyl acetate (certified ACS, Fisher Chemical), octane (reagent grade, Sigma Aldrich), n-hexadecane (99%, Sigma Aldrich).

Nanocrystal Synthesis and Solution Preparation

CdSe QDs were synthesized according to a modified method from that previously reported.[74] 130 mg (1 mmol) CdO powder was loaded into a 100 mL 3-neck reactor along with 16g ODE and 0.6 g OLAC. This mixture was placed under vacuum at 110 °C for 45 minutes. Then it was placed under N_2 flow, heated to 290 °C, and kept there for 5 minutes. The red mixture should turn clear as Cd-oleate forms. The solution was allowed to cool to 100 °C when 2.0 g TOPO and 1.8g HDA (both solids) are added into the reactor. The reactor was placed under vacuum at 110 °C for 15 min, then placed under N_2 and heated to 290 °C. Once the temperature stabilized, a solution of 100 mg (1.3 mmol) Se dissolved in 2 mL TOP was swiftly injected. The reaction proceeded for 2 minutes and was quenched via water bath. The particles were washed 3 times with ethyl acetate and toluene.

The methodology for the CdS shelling process was derived from previously reported work.[45] It requires the synthesis of Cd-oleate as a precursor. Cd-oleate at a concentration of 0.2M in OLAC was prepared by mixing 1.28 g CdO in 31.5 mL OLAC and 18.3 mL ODE in a three-

neck reactor. The mixture is degassed at 110 °C for 1 hr and then placed under N_2 and heated to 160 °C until Cd-oleate forms (~30min) The Cd-oleate is stored in an N_2 glovebox.

To grow the CdS shells, 100 nmol of CdSe QDs are dispersed in 6 mL of ODE in a three-neck reactor and degassed at 110 °C for 1 hr. The mixture is heated to 310 °C. As the temperature increases, injection of two precursors begins when the temperature reaches 240 °C. 0.2 M Cd-oleate and 0.2 M 1-octanethiol in ODE are simultaneously injected at a rate of 0.05 mL/min. Increased injection volume increases the CdS shell thickness. For these particles, the total injected volume of each precursor was 2.5 mL (45 min injection). The particles were washed 3x via ethanol and toluene.

Lastly, the colloidal printing inks were prepared according to a previously reported methodology.[73] CdSe/CdS core/shell quantum dots were prepared as an ink for printing by crashing a known quantity of dots from the stock solution. The crashed pellet was dispersed in 1:1 octane and hexadecane to a volume that puts the optical density of the first excitonic absorption peak at 0.8 in a 1 cm pathlength cuvette.

Nanophotonic Cavity Design and Fabrication

The Si_3N_4 nanobeams were designed for operation in a suspended configuration. The waveguides use 200 nm thick Si_3N_4 and are 15 μm long. For the dielectric-mode cavity design, the cavity region consisted of elliptical holes with a major radius of 132 nm, minor radius 60 nm, and a fixed period of 195 nm. The defect was formed by quadratically tapering the major radii of these holes to 63 nm over the span of 15 periods. The waveguide width was fixed at 600 nm. An additional 20 elliptical holes on either side with the same major radii formed the Bragg mirror regions. According to finite-difference time-domain simulations (FDTD) (Lumerical, Inc), this resulted in a theoretical cavity quality factor of ~20,000 and a mode volume of ~2 ($\left(\frac{\lambda}{n}\right)^3$).

The Si_3N_4 nanobeams were fabricated using 200 nm LPCVD Si_3N_4 on a Si substrate. A 300 nm-thick ZEP520A electron beam lithography resist was spun-coat onto the chip, and electron-beam lithography followed by development in amyl acetate transferred the pattern to the resist. A plasma etch consisting of CHF3/O2 chemistry transferred the pattern to the underlying SiN. After stripping the remaining resist with methylene chloride, an isotropic XeF2 etch was used to etch the underlying Si and suspend the Si_3N_4 nanobeams.

Electrohydrodynamic Inkjet Printing

Electrohydrodynamic inkjet printing was conducted by loading the prepared CdSe/CdS ink into pulled borosilicate glass capillary pipettes with a tip internal nozzle diameter of 1-3 μm. These printheads were manufactured with an inlaid gold electrode along the interior wall of the pipettes that serves to apply a bias near the printing medium. After mounting the printhead into the printer and placing the substrate on a grounded stage vacuum chuck, an alignment process was used to map the designed printing patterns to the orientation of the target substrate. Upon completion, printing was initiated with the following parameters: Bias: 230 V, Amplitude: 50 V, Frequency: 1 kHz.

Photoluminescence Characterization

The Si_3N_4 nanobeams were characterized using cavity-coupled PL both excited and collected directly from the centers of the nanobeams. All measurements were performed in a scanning PL microscopy set-up operating in ambient conditions. For the Si_3N_4 nanobeams without CdSe/CdS QDs, a 445 nm continuous wave laser (CNI Laser MDL-III-445L*)* was focused on the center of the Si_3N_4 nanobeam using a 100x/0.95 NA objective to excite PL from intrinsic Si_3N_4 defects and excite the cavity mode. For Si_3N_4 nanobeams with CdSe QDs, a 532

nm pulsed laser with 10 MHz repetition rate (NKT SuperK FIANIUM*)* was focused on CdSe/CdS QD ink droplets positioned on the center of the nanobeams to measure the cavity mode coupled to CdSe/CdS QDs. The PL spectra were collected by detecting the PL with a Princeton Instruments Isoplane 160 spectrometer with a 1200 lines/mm grating coupled to a Pixis 400 CCD. Lifetime measurements were performed by detecting the PL of CdSe/CdS QDs with avalanche photodiode single photon detectors (Micro Photon Devices PDM) and synchronizing the detector signal with the pulsed laser repetition (PicoQuant TimeHarp 260*)*. In all cases, a 550 nm LP (ThorLabs DMLP550*)* dichroic mirror in conjuction with a 550 nm LP filter (ThorLabs FEL0550) was used to filter out the pump laser.

Acknowledgements

Chapter 1, in full, is a modified reprint of the material published in Advanced Materials Technologies. Gregory G. Guymon, David Sharp, Theodore A. Cohen, Stephen L. Gibbs, Arnab Manna, Eden Tzanetopoulos, Daniel R. Gamelin, Arka Majumdar, and J. Devin MacKenzie, Advanced Materials Technologies, 2024. The dissertation author was the primary researcher and author of this paper.

Chapter 2 Deterministic Printing of Single Quantum Dots

Background

The proliferation of electronic and photonic devices necessitates innovations in precise, scalable, and less wasteful fabrication of nanoscale components. Among techniques that can directly integrate device elements with diverse physical properties and compositions, additive manufacturing through inkjet printing has emerged as a versatile method for depositing picoliter liquid volumes, with applications ranging from graphic printing to advanced microelectronics[92,93] and photonics[31]. Printed electronics are particularly materials-efficient as compared to conventional subtractive processing of electronics[94]. Considering the emissions associated with processing alone, printing of electronics has been modeled to have more than two orders of magnitude lower environmental emissions footprint than conventional approaches[95]. Electrohydrodynamic (EHD) printing advances inkjet methods by employing electric fields, as opposed to mechanical or thermal stimuli, to manipulate fluid inks. EHD printing can readily achieve patterned feature resolutions well below 10 μm (Figure 2.1a)[39,55,68,73,96–100], enable attoliter-scale droplet deposition, and facilitate integration of functional materials onto a variety of substrates. Unlike conventional inkjet droplet formation mechanisms, EHD inkjet uses electric fields acting on ink components to overcome fluid surface tension barriers that limit the feature sizes limits of conventional approaches. This enables nanoscale control over deposit size and placement through a transfer mechanism that requires no moving parts, and is readily scalable into parallel printing modules for higher throughput manufacturing[101,102].

Recently, by leveraging dielectrophoretic (DEP) forces, EHD printing has been shown to form and eject sub-attoliter liquid droplets carrying solids by polarizing the particles themselves in nonuniform electric fields[73,103]. This mechanism generates directional forces on the particles,

driving solid-laden fluid along electric field gradients to allow the formation and acceleration of high surface energy small droplets towards a target substrate. Conventionally, the ink fluid has largely been considered as a continuum of liquid and solid constituents, relying on the reduction of printhead nozzle diameters to reduce droplet volumes and nanoparticle counts[39]. Here, we demonstrate a new regime of EHD printing, acting on sub-zeptoliter, highly-polarizable, single particles dispersed in relatively non-polarizable solvents, to selectively extract and print individual quantum dots (QDs)—a critical milestone for scalable integration of nanoscale materials. These semiconductor nanocrystals, known for their size-dependent properties, are desirable for next-generation technologies, including optical quantum devices[104,105], nano-transistors[106,107], sensors[16], light-emitting diodes[108,109], single-photon sources[21,110], and CMOS circuits[111].

For this study, we selected ligand-dispersed CdSe QDs with colossal CdS shells (80 monolayers) due to their relatively large size (~70 nm in diameter) and high dielectric constant that result in large static electric dipole moments, good dispersion, and optoelectronic stability[112,113]. In the new EHD printing regime explored here, we have defined electric field and waveform conditions, modeled the electric field environment enabling single QD printing, and determined a QD size range for a given applied electric field to enable selective deposition of single nanoparticles. Furthermore, we have employed this EHD printing mechanism, along with spatial positioning and optical alignment hardware, to pattern single QDs in arrays and achieved deterministic placement of single QDs on nanophotonic cavities. We have also characterized the optical properties of the printed QDs and demonstrated, for the first time, single-photon emission from deterministically printed QDs in arrays and coupled to an optical cavity. We propose this new printing approach as a versatile method for selectively depositing single nanoparticles,

offering a transformative pathway for fabricating advanced classical and quantum electronic and photonic devices with nanometer-scale resolution.

Results and Discussion

Figure 2.1b schematically illustrates our EHD printing setup for positioning single QD particles. Printing is initiated by applying a voltage between the electrode-integrated glass capillary printhead and the substrate. This creates an electric field that guides the QDs to the substrate. The top inset for Figure 2.1b shows a fluorescence microscopy (FLM) image of a capillary printhead loaded with dilute colossal QD suspension showing the presence of isolated emitters that include dispersed single QDs. By varying the printhead-to-substrate standoff height and applied voltage, the electric field intensity can be maximized at the tip interface. Colloidal particles in an "ink" composed of oleic acid capped CdSe/CdS core/shell QDs suspended in an apolar solution mixture are then driven to the tip interface by the electric field. This particle mobility is achieved by utilizing a medium with a lower relative permittivity than that of the dispersed particles, which gives rise to a polarization disparity between the two that forces the particles towards regions of high electric field intensity. The QDs used in this work were synthesized via a volumetrically tunable strategy that enables the QD core to maintain its quantum-confined optoelectronic characteristics, while increasing the overall size and dipole moment of the particle in an applied field through the shell design (Figure 2.1c). The tunable polarization is crucial for generating the DEP forces needed to overcome the net interfacial energies of a single particle, especially when factors like electric field intensity and material properties have finite limits, as discussed in the following sections. The colossal core/shell synthesis yields slightly asymmetric, hexagonal, faceted particles that we approximate as spherical for later numerical and analytical estimations, due to their relatively isotropic

morphology[114]. Our simulation shows that the particle asymmetry is not significantly changing the printing behavior here (Figure A4).

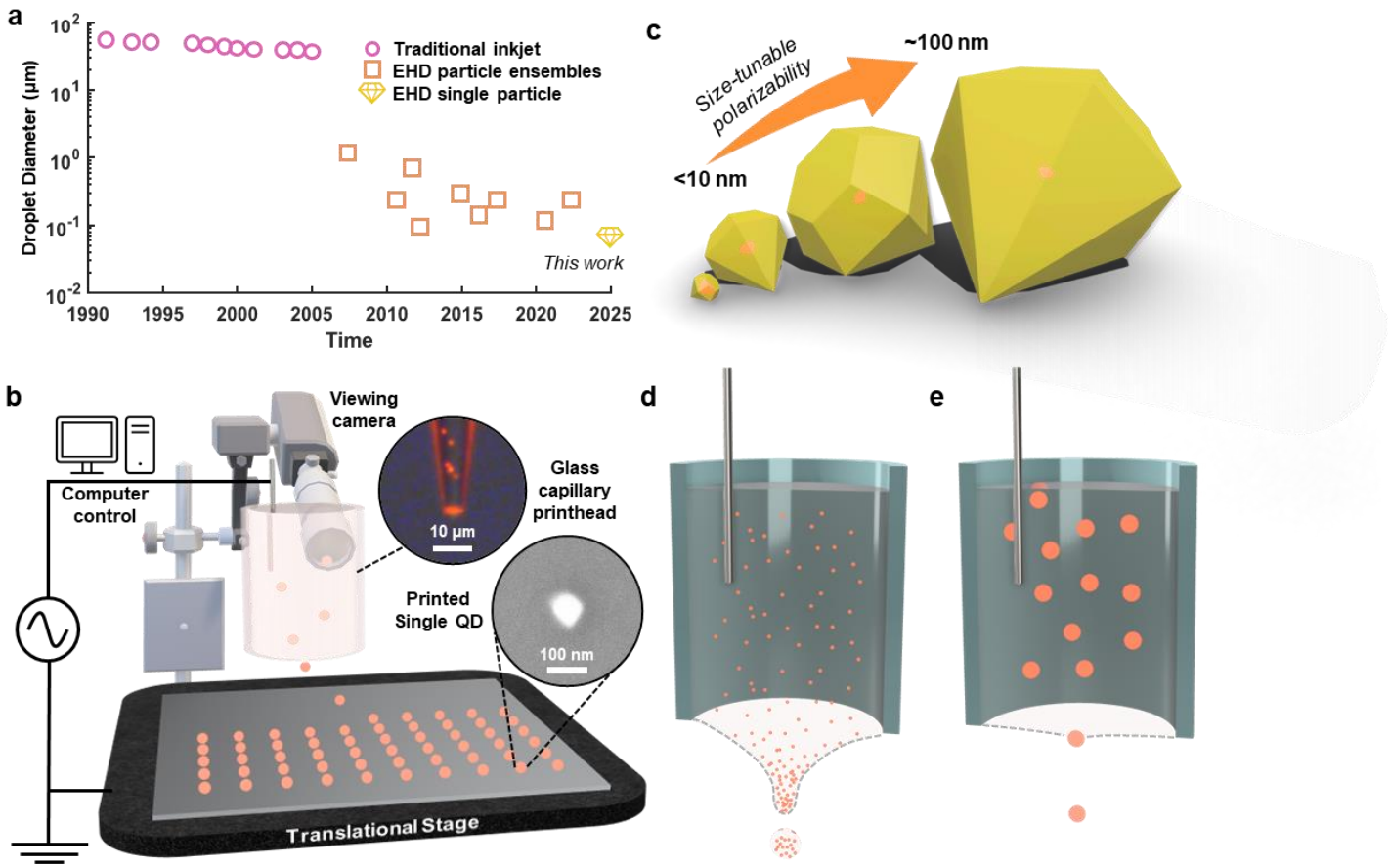

Figure 2.1. Overview of experiment. a, Reported droplet sizes using conventional mechanical inkjet and EHD printing over the past 35 years, along with the results of this work. b, Schematic diagram of the EHD printing setup used here. Top inset: FLM of EHD printhead. Bottom inset: Scanning electron microscopy (SEM) of single EHD-printed QD. c, Graphic representation of CdSe QD cores (orange) with tunable range of hexagonal diamond CdS shell (yellow) diameters. d and e, Bisected illustrations of EHD printheads dielectrophoretically overcoming (d) surface tension to print droplets of particle ensembles and (e) interfacial forces to print singular particles.

In order to determine the optimal EHD printing and material design parameters, we first approach the process of separating an individual nanoparticle from a liquid-solid interface by first principles. Each interface in a three-phase system has an associated energy that quantifies the intermolecular interactions dictating the work to expand said interface. These energies can be

described as the surface free energy (σ_{SG}), surface tension (σ_{LG}), and interfacial tension (σ_{LS}), which correspond to the solid-gas, liquid-gas, and liquid-solid interfaces, respectively. By considering the contact angle (θ_{CA}) at the liquid-gas interface, the values can be related to one another via Young's equation:

$$\sigma_{LS} = \sigma_{SG} - \sigma_{LG}\cos(\theta_{CA}) \tag{2.1}$$

Conventional EHD printing strategies focus on overcoming the energy of surface tension (Figure 2.1d) to generate higher area, reversed curvature liquid-gas interfaces in the form of convex Taylor cones and droplets. Alternatively, to separate a particle from a liquid-solid interface, our focus is on overcoming interfacial tension (Figure 2.1e). This energy determines the work (W) needed to deform the liquid interface around a particle, where ΔA represents the change in interfacial area as the particle passes through the meniscus interface:

$$W = \sigma \Delta A \tag{2.2}$$

The total energy required can be determined by considering the net positive and negative changes in the interfacial area for each interface. For a spherical model, the force (F_{net}) required to overcome the net interfacial forces can then be derived with respect to the translational z-axis, i.e. the printing direction towards the target substrate, where a is particle radius:

$$\frac{dW}{dz} = F_{net} = (\sigma_{SG} - \sigma_{LS} - \sigma_{LG})2\pi a \tag{2.3}$$

We measured the components of interfacial tension through optical tensiometry to determine the F_{net} as a function of particle perimeter (see methods). First, we performed a pendant drop test (Figure A5) to determine the surface tension of the apolar solution, which agrees with previously measured values of the solution's constituents[115]. For the free surface energy of the QDs, we performed a sessile drop test on prepared QD thin films (Figure 2.2a), which also agrees with former analysis of the QD ligand chemistry[116]. We then solved for the

interfacial energy in equation (1), resulting in a value of 6.9 $\pm$ 1.0 mN/m, which allows us to estimate the F_{net} a single particle needs to overcome to print.

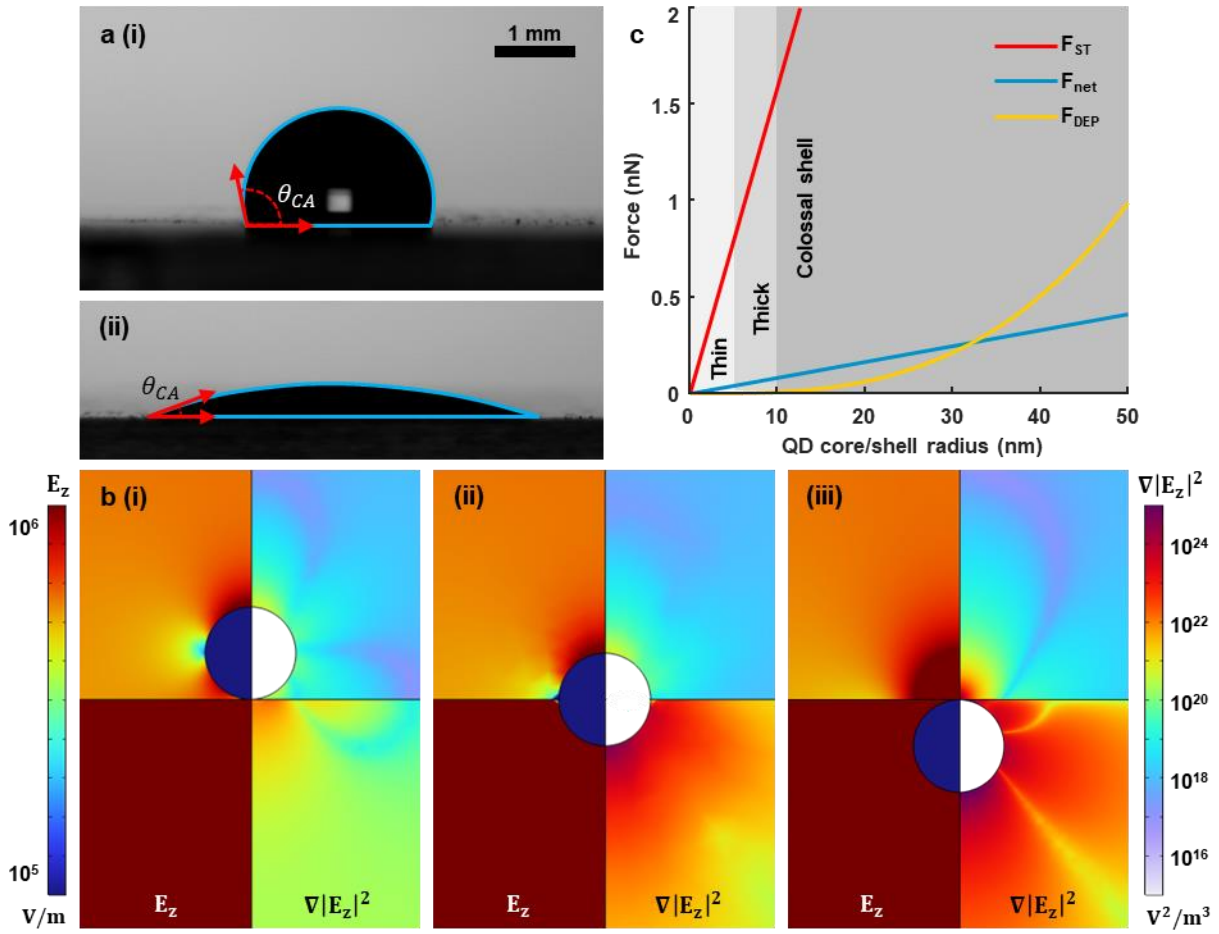

Figure 2.2. Characterization of ink and energy modeling. a, Shadow images of sessile drop shape analysis of (i) water and (ii) octane:hexadecane mixture on CdSe/CdS QD thin film. Sessile droplet outlines (blue) indicate shape profile used for contact angle and surface free energy measurements. b, Electrical COMSOL simulation of spherical particle at the (i) interior solution interface, (ii) halfway through solution interface, and the (iii) exterior of the solution interface. The left side of each plot shows the z-component of the electric field ($\boldsymbol{E_z}$) and the right side shows the z-component of the gradient of the field magnitude squared ($\boldsymbol{\nabla|E_z|^2}$), (the z-axis is normal to the interface). The simulation is symmetrical around the center axis. c, Plot of surface tension force (red), net interfacial forces (blue) and DEP forces (yellow) acting on single particles of various radii. The shaded background indicates the size regime of the CdS shells.

The DEP force (F_{DEP}) of a spherical particle under an applied non-uniform AC field can be solved analytically[117]:

$$F_{DEP} = \pi \varepsilon_m a^3 \Re[k(\omega)] \nabla |E|^2 \quad (2.4)$$

where ε_m is the real permittivity of the medium and $\nabla|E|^2$ is the gradient of the field magnitude squared for the particle. With the complex permittivities of the particle ($\tilde{\varepsilon}_p$) and medium ($\tilde{\varepsilon}_m$), the direction and magnitude of the force is described by $k(\omega)$, the frequency-dependent Clausius-Mossotti factor:

$$k(\omega) = \frac{\tilde{\varepsilon}_p - \tilde{\varepsilon}_m}{\tilde{\varepsilon}_p + 2\tilde{\varepsilon}_m} \quad (2.5)$$

Simply put, when the particle is more polarizable than its respective medium, like in the approach we propose here, the particle moves along the electric field gradients towards regions of high field strength, often referred to as positive DEP force, and displaces the less polarizable solvent medium. For QDs with separate core/shell materials, the real component of $\tilde{\varepsilon}_p$ can be calculated as the volumetric ratio between the shell and core's real permittivities[118–120]. As the shell radius increases past the thin (<5 nm) to the thick (5-10 nm) and into the colossal (10-50 nm) regimes[112], the contribution of the core to $\Re[k(\omega)]$ becomes negligible, asymptotically approaching $\Re[k(\omega)] \approx 0.52$ (Figure A6), assuming a fixed medium permittivity[121,122].

We estimate the $\nabla|E|^2$ at the QD particle at the interface of the printhead's fluid meniscus in our EHD printer to be on the order of $\geq 10^{23}$ V^2/m^3 using a geometric electrical model by numerically solving Maxwell's equations (COMSOL, Figure 2.2b). Using the measured dimensions of the EHD printhead (Figure A7), we simulated the environment around the particle using the maximum voltage bias that our setup can operate at (2 kV). Here, we assume the conductivity of the particle to be similar to CdS thin films, 10^{-7}~10^{-9} Ω^{-1}-cm^{-1}, as the CdS constitutes the majority of the material volume at large shell radii[123–125]. The plotted z-component of the electric field (E_z) shows a high contrast field intensity difference between the

solution and air, which draws the particle towards the higher field intensity. Additionally, the z-component of the gradient of the field magnitude squared plot shows significant field enhancement at the particle, increasing as it passes through the solution interface. Using these estimates, Figure 2.2c compares F_{DEP} to F_{net} and pure surface tension force (F_{ST}). Here, we see that F_{DEP} grows exponentially with increasing particle radius, overcoming net interfacial forces as the particle enters the colossal regime. However, the DEP forces at this size are significantly less than what would be expected to form a liquid droplet of equivalent size from solution if we treated the ink solution as a continuum fluid as in conventional models for EHD inkjet. By comparing the competing forces, we estimate that a minimum QD radius ~32 nm would be sufficient to overcome the interfacial forces to separate a single QD with our measured interfacial energy from the liquid. To be able to extract and print a single QD and maximize the colloidal stability of these QD solutions, we selected a target particle radius of ~35 nm for further experimentation.

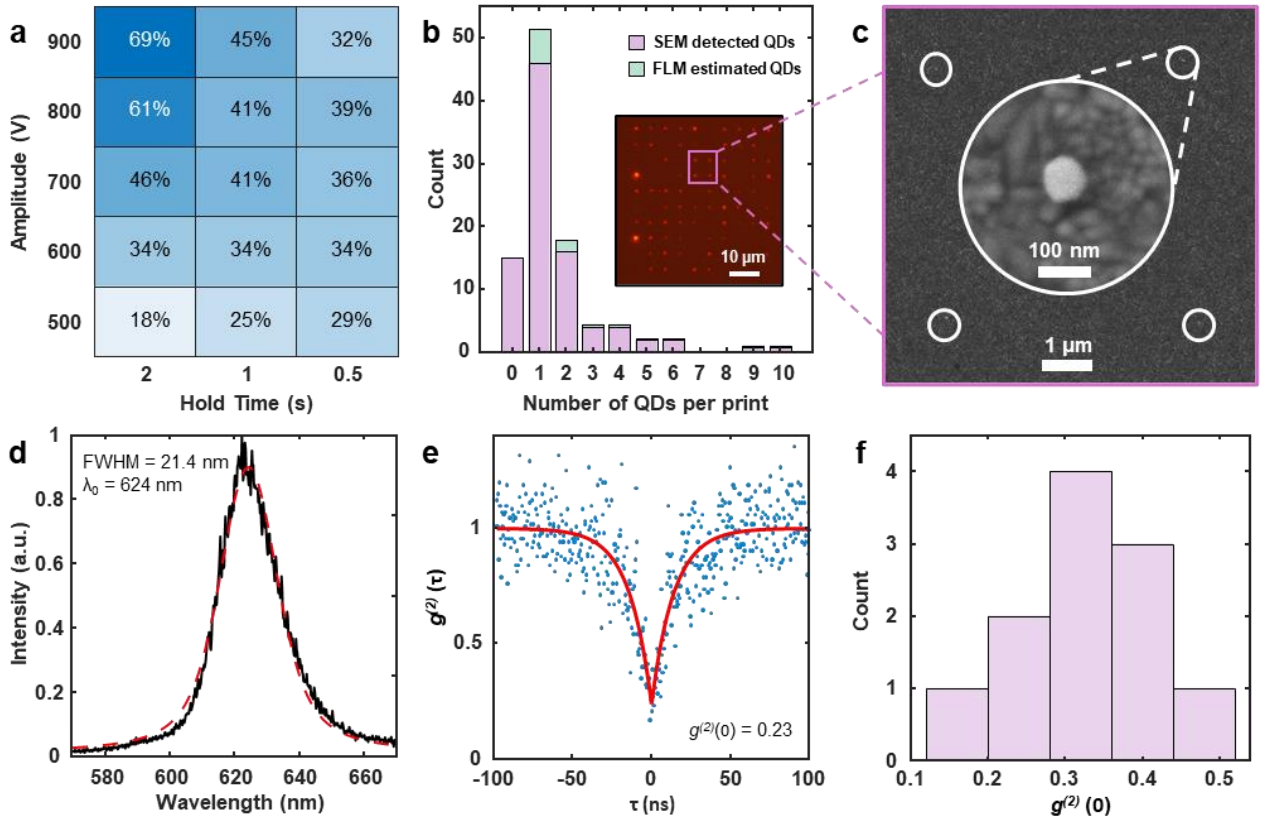

Figure 2.3. Experimental results of EHD printing colossal QDs. a, Effect of drive amplitude on FLM detected print yield as a heatmap of number of prints detected out of a 10 x 10 array of print attempt sites, per parameter configuration. b, Histogram plot of QDs counted per print site for a 10 x 10 array (900 V and 2 s parameter configuration) of attempt sites, as determined by SEM and FLM. Estimated QDs indicate QDs not detected via SEM but were positively-indicated by the FLM (inset). The distribution of estimated QDs is based on the non-zero statistical prevalence QDs per print, per bin. c, SEM image of 2 x 2 array of EHD-printed single QDs on ITO-glass. White circles indicate single QD positions. Inset: SEM image of single QD. d, Plot of single QD emission spectrum (black) and Lorentzian fit (red). e, Second-order time correlation plot (blue) and fit (red) of EHD-printed QD showing single-photon emission, measured at room temperature, with 10 µW excitation (d and e). f, Histogram plot of $g^{(2)}(0)$ measurements on EHD-printed single QDs (n = 11).

To test this estimate, we synthesized CdSe/CdS core/shell QDs with a calculated core radius of 1.8 nm and a designed total average radius of 36 $\pm$ 3.1 nm from 80 CdS shell monolayers (see methods) and dispersed the particles in octane:hexadecane. Figure 2.3a shows the results of a printing trial matrix with this dispersion on Indium Tin Oxide (ITO)-coated glass across a variety of print electrode voltage amplitudes (500-900 V) and hold times (0.5-2 s), with

a fixed bias (1000 V) and frequency (1 kHz). Here, the hold time refers to the period that the amplitude voltage is applied over a target position. Afterwards, using machine vision to count the number of detectable prints (Figure A8), the heatmap shows a gradient of successful QD prints, as determined by FLM. As the hold time and amplitude voltage increase, the number of prints made relative to attempts increases. It should be noted that during this printing process, we could not discern visible meniscus perturbations through high-magnification viewing cameras mounted on the print system, indicating negligible effects of the applied electric fields on the apolar solvent.

Examining the highest print yield array (900 V and 2 s) with SEM (Figure A9), Figure 2.3b summarizes the number of QDs detected per print via SEM and estimated via FLM. These estimations were from print attempt positions that had emission in FLM, but where QDs were not detected during SEM analysis (n = 9). Given the small size and sparseness of the printed QDs in the printed array, the presence of QD luminescence in the FLM was taken as proof of printed QDs at the site. We distributed the undetected emitters based on the statistical prevalence of each non-zero count of QDs detected by SEM, resulting in an overall single particle yield of ~50%. SEM also revealed single particles for positions with no emission (n = 7), indicating that Figure 2.3a slightly underestimates the total yields of prints made. We attribute this lack of emission to either non-radiative recombination from excessive defects in the particles, photobleaching by excitation[126], or QD-excluded CdS aggregates. Figure 2.3c shows a 2 x 2 subarray of single QDs from the larger array. The SEMs show the expected faceted structure consistent with the known morphology of these colossal QDs[112]. We note the lack of any observable drying rings or residue in the vicinity of the QDs. Such features are typically observed when a liquid droplet wets a substrate[127]. The lack of wetting features, in combination with (i) the high surface tension barrier

for liquid droplet formation (Figure 2.2c, red curve), (ii) the calculated dominance of the dielectric forces for QD over the QD interfacial forces at the meniscus (Figure 2.2c, yellow and blue curves), and (iii) negligible interaction of the printing electric fields with the solvents themselves, lays out a new model for EHD printing at the nanoscale. Here, we propose the extraction and directed printing of dry or nearly dry core/shell QDs from apolar solutions with appropriate surface energies, dielectric properties, and electric field environments. Experiments with thin-shelled[103] and smaller colossal-shelled (Figure A10) CdSe/CdS QDs, failed to achieve individual particle printing, again consistent with the proposed model.

Importantly, we also printed single QDs on silicon nitride to improve the signal-to-noise for spectral analysis. Figure 2.3d shows the room temperature photoluminescence (PL) of a single printed QD with an emission peak at 624 nm, and a full-width half-maximum of ~21 nm, consistent with QDs deposited by drop-casting approaches[112] and measured in solution (Figure A11). Second-order correlation ($g^{(2)}$) measurements confirm single-photon emission from printed QDs for the first time. Figure 2.3d shows an example of a QD maintaining its single-photon emissivity ($g^{(2)}(0) < 0.5$) after printing, a critical metric for utilizing these materials as single photon sources in quantum device technologies. Sampling an array of printed single QDs (Figure 2.3f) shows single-photon emission, with a mean $g^{(2)}(0) = 0.33 \pm 0.1$.

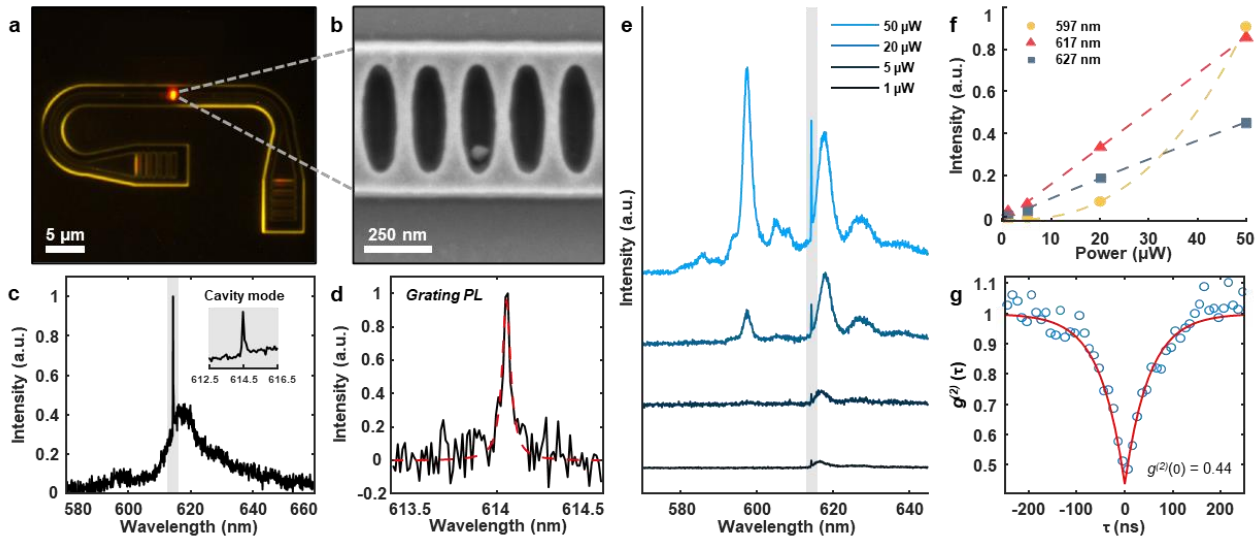

Figure 2.4. Single QD nanophotonic cavity heterointegration. a, Fluorescent microscopy of horseshoe-shaped cavity with single EHD-printed QD. b, SEM image of the cavity region containing single QD. c, Spectrum plot of cavity integrated QD, at 70 K, excited and measured from the top. Inset: Magnified spectrum (shaded) around the cavity mode. d, Spectrum of the pure QD-coupled cavity mode PL to the grating (black) and Lorentzian fit (red) when exciting from the top, measured at room temperature with 10 μW excitation (C and D). e, Power-dependent spectra of QD-coupled cavity at 8 K with the cavity mode region shaded (614 nm), excited and measured from the top. f, Power dependence of 597 nm (yellow), 617 nm (red), and 627 nm (blue) peak intensities at 8 K, with power-law fits (dashed lines). g, Second-order time correlation plot (blue) and fit (red) of cavity-coupled QD, excited (10 μW) and measured from the top at room temperature.

To demonstrate the utility of high-resolution single QD printing, we designed and fabricated a horseshoe-shaped nanophotonic cavity with a resonant frequency of ~614.5 nm and a monolithic waveguide structure that directs emission to rectangular gratings at each end. Applying the strategy described above, we printed a single QD in the center of the cavity. Figure 2.4a shows a FLM image of the emission from the single QD coupling to the waveguide and scattering from the gratings. SEM inspection of the print site (Figure 2.4b) confirms the presence of the single QD by identifying the characteristic hexagonal diamond-shaped colossal QD in one of the cavities' central elliptical wells.

The PL spectrum from the cavity-integrated QD in Figure 2.4c reveals the coupling between the cavity's sharp resonant mode and a broad QD emission at 70 K, a condition chosen

for its high emission intensity (Figure A12). Examining the narrow spectrum around the cavity mode (Figure 2.4c, inset) is consistent with a modest Fano interference, indicated by the characteristic Fano line shape[128], which is more apparent at room temperature (Figure A13). Measuring the room temperature photoluminescence from the cavity grating, at either end of the horseshoe, isolates emission coupled to the cavity mode. Figure 2.4d shows this sharp Lorentzian mode, with a quality factor of 12,500, measured from the Lorentzian fit linewidth over the center wavelength. Similar to our printed arrays, photobleaching also occurred in other single QD-integrated cavities, resulting in only the emission from the SiN background and cavity mode (Figure A14).

We measured the QD-cavity system at 8 K across multiple excitation powers (1-50 μW) to examine the broadened tail emission. Figure 2.4e shows the separation of the broader emission into an excitonic peak (617 nm) and its phonon sideband (627 nm). At higher power (>5 μW), we identify the emergence of a secondary high-energy peak (597 nm), which we attribute to a multi-excitonic transition, accompanied by its own phonon sideband (605 nm). The observed single excitonic and phonon sideband emission is consistent with non-cavity QDs (Figure A15) and the literature[129], at low temperature. As shown in Fig. 4f, the exciton and phonon sideband scale nearly linearly with excitation power. The high-energy peak is highly non-linear, with an exponent of 2.5, suggesting a multi-excitonic origin. Lastly, a $g^{(2)}(\tau)$ measurement of the QD-cavity at room temperature (Figure 2.4f) shows the coupled system maintaining its single-photon emission.

Conclusion

Colloidal QDs have been discussed for quantum optoelectronic applications since their inception yet have largely been outside of practical considerations due to the challenges

associated with their integration into devices. Here, we have demonstrated the first additive nanomanufacturing strategy for deterministically positioning single QDs that exhibit single-photon emission. Not only does this approach allow high throughput printing of large arrays of QDs at room temperature, without resorting to vacuum processing or lithography, but it also allows for the positioned deposition of QDs into prefabricated nanophotonic elements such as high-Q cavities. We propose that this printing is enabled by a new mechanism for electrohydrodynamic printing: dielectrophoretic expulsion of essentially dry, highly polarizable single particles from a relatively non-interacting solvent medium. This mechanism requires particles with sufficient dielectric contrast from the solvent, which can be realized with typical semiconductor nanocrystals at sizes that are now synthetically achievable. While we used colossal-shelled (~70 nm) CdSe/CdS particles here, we estimate the method should be applicable to a range of other colloidal nanoparticles, from halide perovskites, to nanodiamonds, opening the door to a scalable, contactless, zero-wasted additive nanomanufacturing process that can be conducted at ambient conditions to enable the positioning of single discrete colloidal QDs. These results represent significant progress in realizing scalable photonic qubit platforms and the future development of quantum optoelectronics. We also believe this represents a step forward for the additive manufacturing of materials, where low-waste printing processes can match and even exceed the capabilities of conventional subtractive and complex semiconductor fabrication processes.

Experimental Methodology

CdSe QD Synthesis

The synthesis of colossal CdSe/80CdS QDs (CdSe with 80 monolayers (ML) of CdS) was conducted according to methods reported previously[112]. The wurtzite CdSe core synthesis

started with adding TOPO (3 g), CdO (0.06 g), ODPA (0.28 g), and a magnetic stir bar to a 15 mL three-neck round-bottom flask secured with a septum, a thermowell equipped with a thermometer, and a condenser. The flask was put under vacuum for 30 min at 100 °C, then was refilled with N2. The temperature was then set to 375 °C. A dropwise addition of TOP (1.5 mL) was done while the temperature was ramping up from 320 to 370 °C. When the temperature was at 375 °C, a pre-prepared solution of Se powder (0.058 g) dissolved in TOP (0.4 mL) was quickly injected. After 45 s, the flask was quickly cooled to room temperature with forced air to yield CdSe QDs. The QDs were purified in a glovebox by centrifugation with methyl acetate/hexane and were stored in hexane.

Shelling of CdSe with CdS

ODE (6 mL) was added into a 25 mL three-neck round-bottom flask secured with a septum, a thermowell equipped with a thermometer, and a condenser, which was put under vacuum at 110 °C for 60 min, then refilled with N2 gas. An amount of CdSe core in hexane (typically 5–100 nmol) was added to the flask. Hexane was completely removed by evacuating the flask 110 °C for 30. The flask was then heated to 310 °C. When the temperature was at 260 °C, 0.2 M $Cd(oleate)_2$ and 0.2 M 1-octanethiol solutions were slowly injected into the reaction flask using a dual-syringe pump with the rate of 3 mL/h. The volumes of the shell precursors were calculated to achieve 30 MLs of CdS shells on QD cores with a diameter of ~3.5 nm. After the injection finished, the reaction was annealed at 280 °C for 2 h, then cooled down to 60 °C. Without purification, a portion of the yellow CdSe30CdS solution was transferred to a different 3-neck round-bottom flask for another shelling step that targeted additional 20 CdS MLs to achieve CdSe50CdS using the same shelling procedure. This step was repeated one more time to achieve CdSe80CdS. The final product was purified in a glovebox with hexane and then stored

in hexane. Detailed calculations of shell precursor amounts were described in a previous report[112].

QD Ink Preparation

The QD ink was prepared by evaporating a hexane-based QD solution under vacuum at 100 ºC for 30 min, yielding ~3 mg of bright yellow QD powder. The resulting powder was subsequently dispersed in 10 mL of a 1:1 octane:hexadecane mixture through stirring at 80 °C for 1 h, followed by sonication 1 h.

Pendant Drop Tensiometry

The video image was calibrated to the outer diameter of the dispensing syringe of a Krüss drop shape analyzer to establish the scale and obtain accurate drop dimensions. The shape of the drop was then analyzed through grayscale shadow image processing. A shape parameter was adjusted iteratively by a Young-Laplace numerical model until the computed drop shape matched the observed one. Finally, the surface tension was calculated, based on the solution density and the optimized shape parameter, to be 25.3 ± 0.3 mN/m.

Sessile Drop Tensiometry

A substrate for the sessile drop tensiometry was prepared via spin coating CdSe/CdS on a glass substrate. Using a Krüss drop shape analyzer, a drop was deposited onto the solid sample, and its image was captured using a camera, then processed through drop shape analysis software. The drop's contour was first identified using grayscale shadow image analysis. Next, a geometric model was applied to fit the identified contour. The contact angle was determined as the angle between the fitted drop shape and the surface of the sample. These were determined as $92.3° \pm 2.0°$ and $18.5° \pm 2.9°$ for water and 1:1 octane:hexadecane, respectively. After the drop shape and contact angle were measured, the surface free energy of the solid sample was calculated,

using a combination of contact angles from multiple probe liquids (water and 1:1 octane:hexadecane) with known surface tensions, to be 30.8 ± 1.0 mN/m.

Finite Element Analysis

Simulation was performed with the electric current (EC) package within the AC/DC Module using COMSOL Multiphysics. Permittivity and conductivity of the materials were used to perform the simulation. Physical dimensions of the components were modeled after micrographs (printing nozzle), SEM characterization (quantum dot) and measured substrate thickness. A source voltage of 2000 V was used as a stimulus to the electrode voltage, and the printing bed was used as the reference ground for the applied voltage, both analogous to the actual printing setup. A 2D axial rotationally symmetric simulation was performed for the analysis. A flat meniscus was assumed for the liquid-gas interface.

Electrohydrodynamic Inkjet Printing

Electrohydrodynamic inkjet printing was conducted by loading the prepared CdSe/CdS ink into pulled borosilicate glass capillary pipettes with a tip internal nozzle diameter of ~5 μm. These printheads were manufactured with a tungsten electrode filament integrated inside this pipette. After mounting the printhead into the printer and placing the substrate on a grounded stage vacuum chuck, printing could be initiated. For the nanophotonic cavity, an alignment process was used to map the designed printing pattern to the orientation of the target substrate. Upon completion, printing was initiated with the following parameters: bias: 1000 V, amplitude: 900-1000 V, frequency: 1 kHz, hold time 1-2 seconds.

Photoluminescence Characterization of Bare Substrate QD

Single-particle characterization was performed in air using a custom-built scanning PL set-up. A 532 nm continuous-wave laser (Laserglow Technologies 532 nm DPSS Laser) was

focused on the particles with a 100× (NA 0.95) dry objective lens with a typical excitation power of 10 μW. The laser spot position was controlled via a steering mirror (Newport FSM-300–01). The collected PL was filtered through both a 550 nm long-pass filter and a bandpass filtered centered on 618 nm with 50 nm bandwidth. The collected PL was fiber-coupled either to a spectrometer (Princeton Instruments Isoplane 100) to collect the single-particle spectrum or through a 50:50 fiber splitter to a pair of avalanche photodiodes (MPD-PDM) to collect the $g^{(2)}$ spectrum. For the $g^{(2)}$ spectra, the time correlation was performed via a time tagger (PicoQuant TimeHarp 260).

Nanophotonic Cavity Fabrication

The SiN nanobeam cavities were designed for operation on a SiO_2 substrate with no top cladding in 220 nm thick SiN. The cavity was formed by punching a one-dimensional array of elliptical holes in a 550 nm wide SiN waveguide. The dimensions of the elliptical holes were fixed to a major diameter of 411 nm and a minor diameter of 98 nm. Each half of the cavity consisted of 10 elliptical holes that quadratically tapered from a period of 184 nm to 190 nm. An additional 20 elliptical holes with a period of 193 nm were placed on either end to form the cavity mirrors. According to FDTD simulations, this resulted in a cavity mode at 618 nm with quality factor ~4 x 10^5 and mode volume ~ 2 $(\lambda/n)^3$. To fabricate the nanobeam cavities, 100 kV ebeam-lithography was used to transfer the pattern to a positive-tone ebeam resist. The pattern was then etched into the SiN thin film using a fluorine-based plasma etch.

Photoluminescence Characterization of Cavity-Integrated QD

Measurements were performed in a confocal setup operating in ambient conditions. Green continuous wave 532nm laser light (LaserQuantum opus532) was passed through a 532 dichroic mirror (Chroma ZT532RDC) focused onto the center of the cavity using a 40x/0.6 NA

Olympus objective, with a 1 μm spot size. A 580LP was used to filter out excitation light and PL went to a Princeton Instruments 300 grooves/mm grating spectrometer (SpectraPro HRS-750) coupled to a Pixis CCD (PIXIS: 100BR_eXcelon). Confocal scans were performed using a SPCM (Excelitas SPCM-AQ4C) coupled to a NIDAQ (BNC-2110). g2 was measured by going through a 40:60 fiber beam splitter and a timetagger (Swabian Instruments Timetagger Ultra). All low temperature measurements were done with a Montana cryostat (cryostation S-series) operating at 8K. Peaks in Figure 2.4e were integrated and fit to a power law $I = aP^b$(Figure 2.4f), with the emission intensities scaling with excitation power (P) : excitonic (P^1), multi-excitonic (P^2 or higher), and phonon-assisted (P^1 or higher).

Acknowledgements

Chapter 2, in full, is currently under review for publication of the material. Gregory G. Guymon, Hao Nguyen, David Sharp, Tommy Nguyen, Henry Lee, Brandi Cossairt, Arka Majumdar, Kai-Mei Fu, and J. Devin MacKenzie. The dissertation author was the primary researcher and author of this paper.

Chapter 3 Femtoscale Reactor for Single Nanocrystal Synthesis

Background

Semiconductor nanocrystals (NCs) are a leading material of interest for quantum optoelectronics due to their exceptional photonic properties. Perovskites in particular have drawn the attention of chemists and physicists alike for their high photoluminescent quantum yield, narrow emission line widths, wide color gamut, and long carrier lifetimes.[47] Furthermore, their solution processability makes them a highly desirable candidate for scalable integration into optoelectronics such as light-emitting diodes,[130,131] photodetectors,[61] and photovoltaics.[132] Their properties make them especially attractive for nanophotonic applications.[133,134] However, deterministically positioning and integrating them remains a serious challenge.

For colloidal perovskite NCs, templating methods have remained as a popular methods for integration.[135] This method involves laying a prefabricated template onto the substrate of interest, depositing a colloidal solution on top, and then removing the template to leave behind the material of interest. This strategy is challenging for deterministic low-to-single particle integration however, as it relies on dispersing low concentrations of NCs in solution and hoping that NCs settle in the template positions of interest. Recently, a giant shelling method for II-VI semiconductor NCs improved the likelihood of single particle positioning in templates by preventing other particles from settling into an already filled template position.[30] However, perovskites struggle with shell growth due to rapid ion migration and surface defect formation, with no large shelling strategy having been demonstrated to the best of our knowledge.[136,137]

Thus, instead of positioning already synthesized perovskite NCs, growing them at positions of interest is the alternative strategy. Templating strategies have been extended in this regime of synthesis, by designing the templates as wells for solution to nucleate and grow

nanocrystals (~50 nm).[42] While this strategy demonstrates large-area scalability for deterministic nanocrystal synthesis, the strategy requires the exposure of the whole-area to the solution by drop casting and spin coating. Additionally, the template wells are a requirement for nanocrystal synthesis, limiting the nanophotonic architectures compatible with the process.

Recent advances in inkjet printing have enabled the size-tunable synthesis of single perovskite crystals at the submicron scale.[138] This precise control is largely achieved by regulating the droplet volume ejected by the printhead, allowing reactions to take place on picoliter scales. Moreover, innovations in cosolvent strategies have further refined the controlled growth of these crystals. One such approach involves a secondary, low-vapor-pressure cosolvent that becomes supersaturated as the primary perovskite solvent evaporates. This method prevents premature precipitation and facilitates the formation of the desired crystalline structure during annealing, offering greater control over crystal quality and uniformity.[139]

Although conventional inkjet printing techniques are highly scalable for the synthesis of submicron perovskite crystals, they are constrained by droplet sizes (>10 μm), limiting their use in high-resolution nanophotonics applications.[140] To address these limitations, electrohydrodynamic inkjet (EHDIJ) printing has emerged as a powerful method for generating nanoscale droplets on-demand. In this technique, a high-strength electric field is applied between the printhead and a grounded substrate, polarizing the solution meniscus. The resulting electrodynamic forces pull the meniscus along the field direction, forming a Taylor cone. As the cone elongates, a field-focusing effect further narrows its tip, enabling the production of droplets that are several orders of magnitude smaller than those from conventional inkjet systems, in the femtoliter to attoliter range.[51,73,103] This allows for precise material deposition, essential for nanoscale photonic integration.

Herein, we demonstrate the additive deterministic synthesis of perovskite nanocrystals through an EHDIJ cosolvent printing strategy.

Results and Discussion

For femtoscale reaction of single nanocrystals, a cosolvent $CsPbBr_3$ perovskite ink was prepared for EHDIJ printing. First, equimolar parts CsBr and $PbBr_2$ were dissolved at room temperature in dimethyl sulfoxide (DMSO) at a solution molarity just below the solubility limit of 0.5 M.[132] After complete dissolution, an aliquot was taken to redisperse into n-cyclohexyl-2-pyrrolidone (CHP) to prepare the cosolvent ink. Subsequent aliquots were then taken and redispersed into similarly prepared plain DMSO:CHP inks to reach solution molarities of interest ($\leq$10 mM). The cosolvent ratios were determined through printing stability trials, decreasing the ratio of DMSO to CHP to reduce unintended solvent evaporation at the printhead tip that would cause premature nucleation and growth of $CsPbBr_3$. This premature growth would cause clogging and other electrohydrodynamic phenomena such as twin jetting and electro-spraying that is undesirable for this experiment (Figure A16).

Figure 3.1A provides a schematic overview of the EHDIJ printing process. Here, the $CsPbBr_3$ DMSO:CHP ink is loaded into a borosilicate glass pulled pipette printhead for printing. Printing is initiated by applying a voltage bias between the grounded substrate and the printhead electrode, polarizing the surface of the solution meniscus and forming a Taylor cone along the direction of the electric field. The voltage bias is bumped from on/off to generate single droplets on demand at positions of interest by intentionally destabilizing the Taylor cone. In this experiment, the substrate is treated with a vapor coated self-assembled monolayer (SAM) of trichlorosilane to improve the hydrophobicity of the substrate and minimize droplet spread.

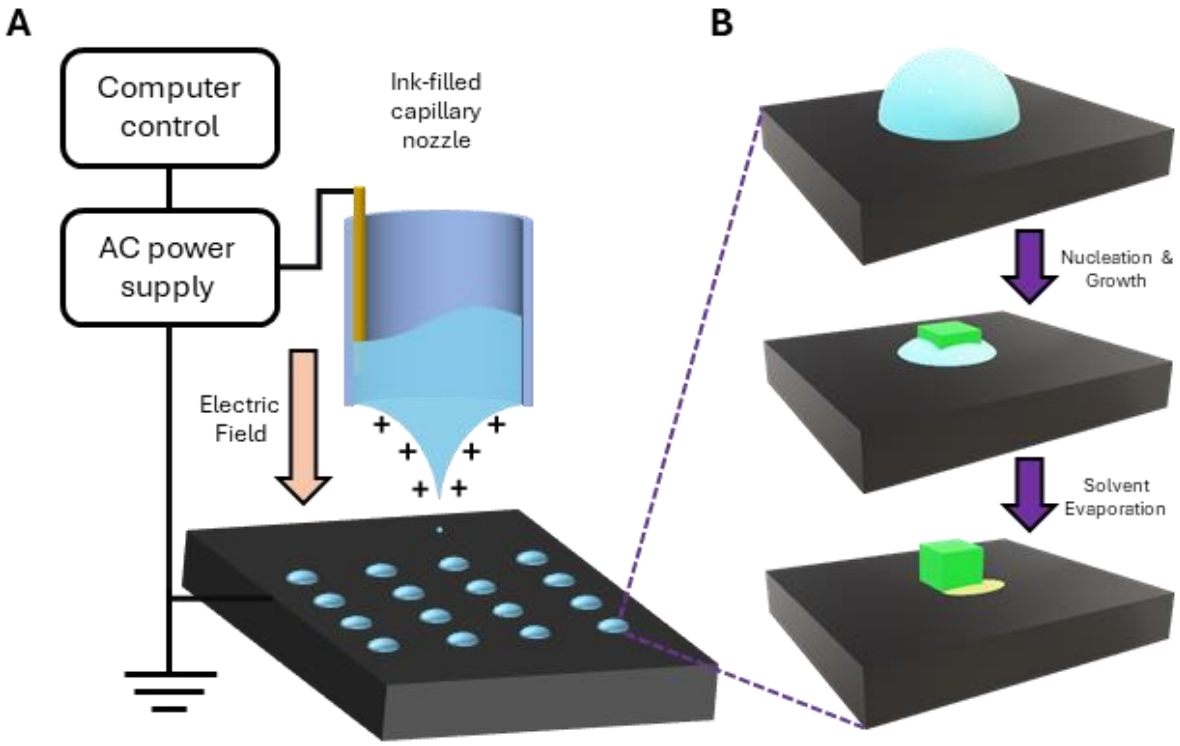

Figure 3.1. Schematic overview of experiment. (A) Diagram of the EHDIJ printing process for perovskite precursor solution. (B) Illustration of the perovskite precursor solution under annealing process to grow single crystals.

Following EHDIJ printing of the perovskite precursor solution, the samples undergo annealing to accelerate the evaporation of CHP and facilitate the controlled crystallization of $CsPbBr_3$ nanocrystals. As shown in Figure 3.1B, the rapid evaporation of DMSO leads to supersaturation of the CHP solution, triggering nucleation and subsequent crystal growth. During this process, as the solvent continues to evaporate, the shrinking droplet concentrates excess ions around the already nucleated crystal, further driving growth while suppressing the formation of additional nuclei. The presence of the SAM aids in this process by reducing droplet pinning, enabling uniform recession of the droplet and promoting more controlled crystal growth.

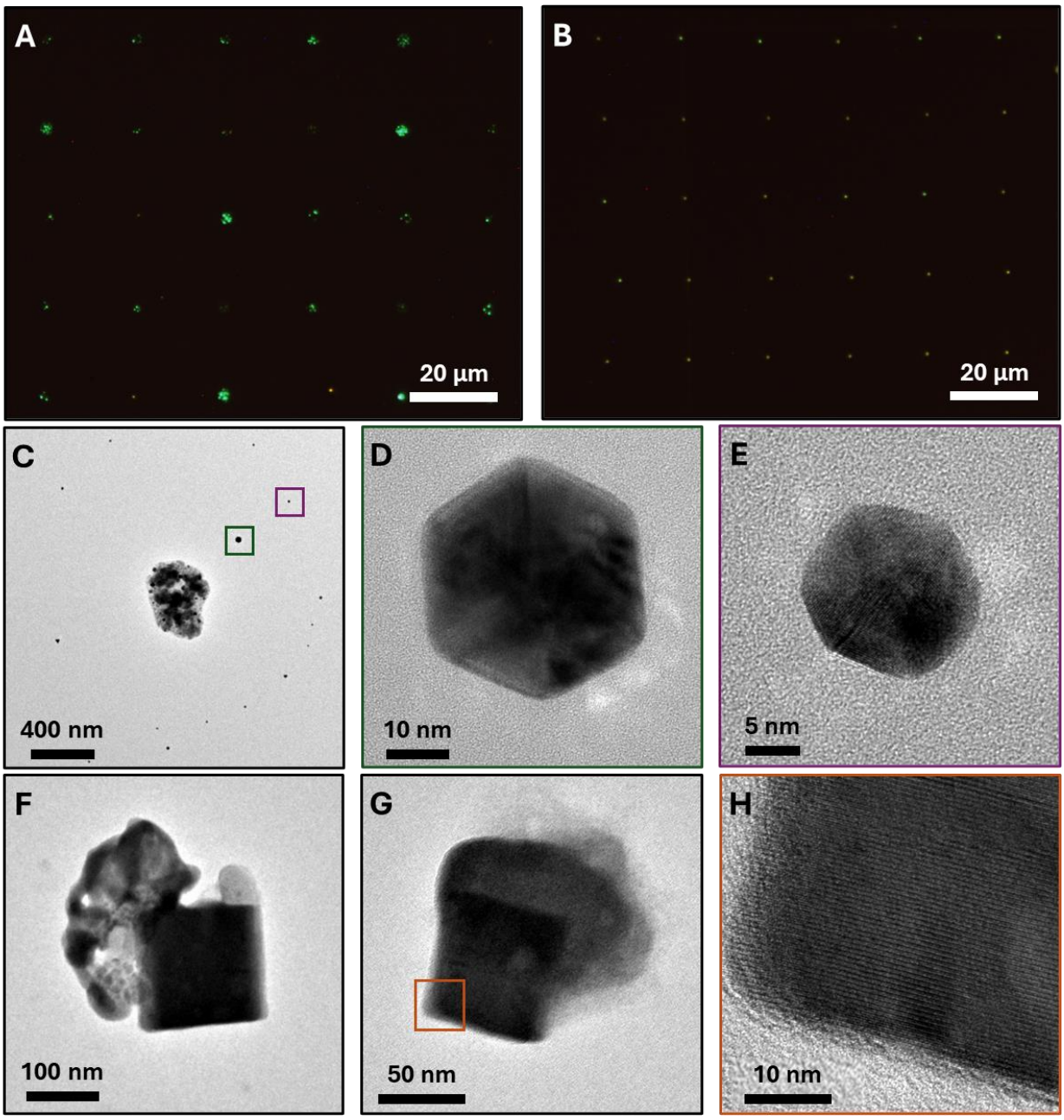

Figure 3.2. Microscopy analysis of EHDIJ printed perovskites. (A) FL microscopy of 0.5 mM $CsPbBr_3$ 1:9 DMSO:CHP print array, annealed without vacuum. (B) FL microscopy of 0.5 mM $CsPbBr_3$ 1:39 DMSO:CHP print array, annealed without vacuum. (C) TEM of single print from 0.5 mM $CsPbBr_3$ 1:39 DMSO:CHP print array. Green and purple boxes indicate subsequently inspected satellite nanocrystals. (D) TEM of large satellite nanocrystal. (E) TEM of small satellite nanocrystal. (F) TEM of 2.5 mM 1:39 DMSO:CHP print, vacuum annealed. (G) TEM of 0.5 mM 1:39 DMSO:CHP print, vacuum annealed. Orange box indicates subsequently inspected area. (H) TEM inspection of lattice fringe of single $CsPbBr_3$ nanocrystal.

To see how the cosolvent ratio plays a role beyond print stability, Figure 3.2A and Figure 3.2B compare printed and annealed $CsPbBr_3$ inks of equal molarity but with DMSO:CHP ratios of 1:9 and 1:39, respectively. Annealed on a hotplate, the former ink produces mostly distinct large area prints that form into films and/or visually separated large crystal islands. Increasing the ratio of CHP from 90% to ~97% reduces the more volatile DMSO from the cosolvent and produces smaller sized prints, post-annealing, with greater consistency than the former cosolvent ratio, with no visual indication of film or large island formation. It should be noted that despite the smaller size of the annealed print, the volumes printed where the same. Examining these smaller prints with TEM (Figure 3.2C) reveals that they are not forming as single crystals, but rather compacted cores of multiple sub-100 nm sized NCs (Figure A17). These cores are surrounded by NC satellites, with edge lengths ranging from ~15 nm (Figure 3.2D) to sub-10 nm (Figure 3.2E).

To reduce the formation of the core/satellite structure, perovskite inks were annealed under vacuum conditions post-printing. Using the 1:39 DMSO:CHP cosolvent ratio, Figure 3.2F shows a single printed feature using 2.5 mM ink, yielding a large nanocrystal with a ~150 nm edge length. Figure 3.2G shows another nanocrystal grown from a 0.5 mM ink, with a ~60 nm edge length. Neither of which formed satellite NCs when the surrounding area was inspected. Both printed NCs, as well as the core structure in Figure 3.2C, show a residue around the particles that appear to be inorganic based on it's dark appearance. Given the known constituents of the perovskite inks, it is assumed that this is unreacted precipitates, either from stoichiometric unbalances or too-rapid solution evaporation. The vacuum is believed to reduce ambient pressure around the droplet, promoting a more spherical morphology. This geometric change decreases the droplet's surface area and minimizes substrate contact points that typically act as nucleation

sites for multiple crystals. Although vacuum conditions lower the solvent's boiling point and potentially accelerating evaporation, this tradeoff appears to favor the formation of isolated single nanocrystals. The balance between suppressed nucleation and enhanced evaporation may be key to achieving spatially deterministic nanocrystal synthesis. Closer inspection of the nanocrystal structure in Figure 3.2H shows the ordered lattice structure characteristic of perovskite nanocrystals. Electron diffraction of this area reveals the orthorhombic crystal structure (Figure A18), expected for the annealing conditions applied.[141]

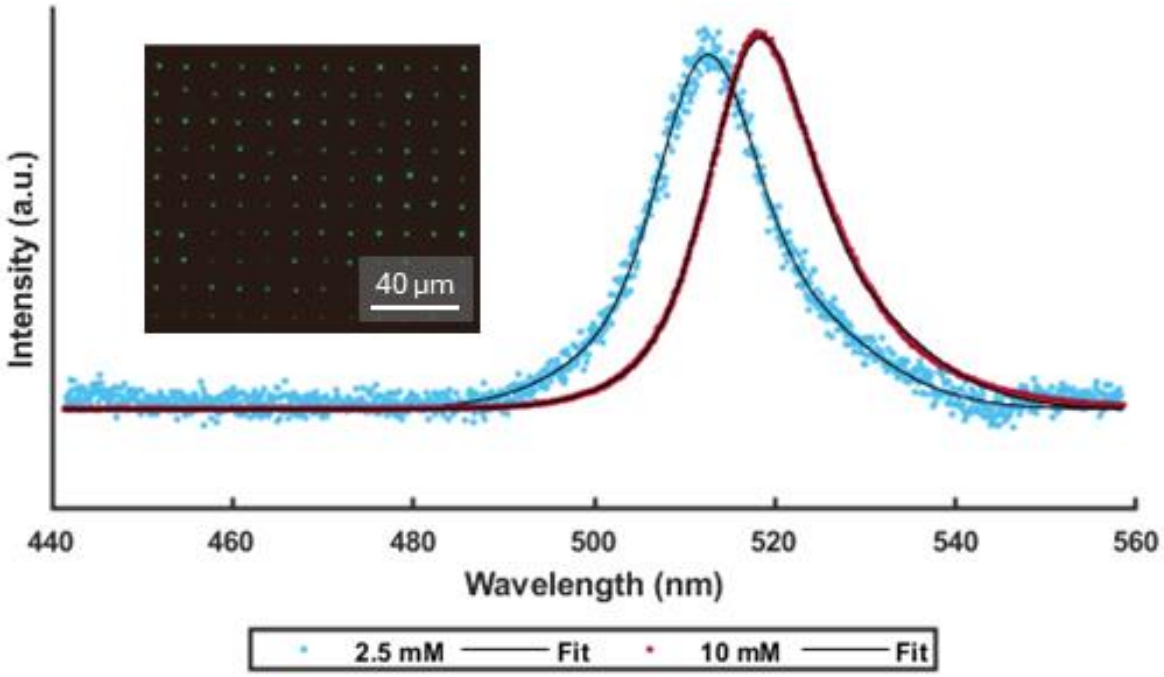

Figure 3.3. Spectral analysis of EHDIJ printed perovskites. Plot compares the normalized photoluminescence spectrum of crystals grown from 2.5 mM and 10 mM $CsPbBr_3$ ink. Inset image: Florescent microscopy of EHDIJ printed 10 mM $CsPbBr_3$ crystal array.

When measuring perovskite crystals grown with photoluminescent analysis, Figure 3.3 shows the comparative results of 10 mM and 2.5 mM 1:39 DMSO:CHP vacuum-annealed $CsPbBr_3$ prints. The crystal shape of the 10 mM sample was more easily characterized with AFM than TEM (Figure A19) due to its larger size. As the concentration of perovskite precursor is decreased, a proportional reduction in crystal size is expected. Examining the spectrums of the

two samples highlight two indicators that support this expectation. First, while the calculated 15.3 nm full-width half-maximum (FWHM) of the spectrums remain the same, the 2.5 mM print spectral peak (512.6 nm) is blue shifted from the spectral peak of the 10 mM print (518.5 nm). This shift is typically associated with the increase in bandgap energy due to quantum confinement. While most often reserved for describing optical behaviors of quantum dots (QDs), this shift has been reported for up to submicron crystals (~1 μm).[142] Other contributions to the shifting bandgap with size could be the effect of crystal lattice strain and the relative amount of surface defects that are known to affect optical properties of nanocrystals.[143,144] Secondly, the increase in noise-to-signal for the same measurement time, as the concentration decreases, shows weaker emission, which indicating a smaller single crystal.

Conclusion

Here, EHDIJ printing was demonstrated as a facile method for deterministically synthesizing both single $CsPbBr_3$ NCs and satellite rings of QD-sized NCs. This was achieved through EHDIJ printing femtoscale cosolvent solutions to maintain a stable dissolution while promoting controlled growth. By reducing the reaction volume and controlling the precursor concentration, nanocrystal size can be tuned. Further optimization of the stoichiometry and/or annealing conditions need to be done to reduce the unreacted precipitation. Additionally, investigation into reducing the precursor concentration to potentially achieve single nanocrystals that approach strong quantum confinement is highly warranted. Overall, this work serves as a motivating platform for further research into nanocrystal synthesis for future quantum optoelectronic applications.

Experimental Methodology

Perovskite Solution Preparation

Perovskite solutions were prepared by dissolving equimolar parts of CsBr and $PbBr_2$ in DMSO at 0.4 M and stirred overnight. Aliquots of the solution were dispensed into CHP at the multiple referenced DMSO:CHP ratios to prepare the cosolvent and stirred overnight. Further dilutions were prepared from aliquots for the described concentrations.

Electrohydrodynamic Inkjet Printing

Electrohydrodynamic inkjet printing was conducted by loading the prepared $CsPbBr_3$ DMSO:CHP ink into pulled borosilicate glass capillary pipettes with a tip internal nozzle diameter of 1-3 μm. These printheads were manufactured with a tungsten electrode filament integrated inside this pipette. After mounting the printhead into the printer and placing the substrate on a grounded stage vacuum chuck, printing could be initiated. Printing was initiated with the following parameters: bias: 0 V, amplitude: 100-150 V, frequency: 1 kHz, dwell time 10 milliseconds. For spectroscopy measurements, samples were printed on silicon substrates with a vapor coated trichlorosilane top surface. For TEM measurements, samples were printed on SiN window TEM grids that were prepared with a sputter coated with a layer of carbon and vapor coated with tricholorosilane on the top surface.

Annealing

Prints were annealed ~15 minutes after printing under vacuum and ambient conditions at 100-140 °C. Under vacuum conditions, the active vacuum pressure was set to ~30 inHg.

Acknowledgements

Chapter 3 contains work-in-progress material being prepared for publication. Gregory G. Guymon, Eden Tzanetopoulos, Tommy Nguyen, Daniel R. Gamelin , Kai-Mei Fu, and J. Devin MacKenzie. The dissertation author was the primary researcher and author of this work.

Outlook and Conclusion

This dissertation has introduced and demonstrated novel nanomanufacturing techniques that address critical challenges in the fields of quantum optoelectronics and photonic device integration. By leveraging electrohydrodynamic inkjet printing, a scalable, additive, and contactless process, we have shown how it is possible to overcome the limitations imposed by traditional material integration techniques. Through the chapters of this work, we explored the use of EHDIJ printing to integrate quantum materials into complex photonic architectures, position single quantum emitters with nanoscale precision, and synthesize single perovskite nanocrystals on-demand. Each of these contributions serves as an important step toward the realization of scalable, deterministic quantum optoelectronic platforms.

Looking ahead, the advancement of quantum technologies will depend heavily on continued improvements to the tools and techniques used in their fabrication. The ability to precisely position quantum dots, control nanocrystal growth, and heterointegrate functional materials with photonic devices opens the door to a wide range of new applications, from quantum computing to secure communications. However, as demonstrated in this work, there are still key challenges to address. Enhancements in printhead engineering, solvent design, and emitter quality will be essential for further refining device performance. Interdisciplinary research will be necessary to overcome these hurdles, involving collaborative efforts across materials science, physics, chemistry, and engineering.

In conclusion, the work presented in this dissertation sets the foundation for future developments in quantum optoelectronics. EHDIJ printing provides a flexible and scalable manufacturing strategy that can be applied to a diverse array of quantum materials and device architectures. By addressing the fundamental issues of material integration and scalability, this

research brings us closer to realizing practical quantum technologies that could redefine fields such as computation, sensing, and communications. Future efforts will build upon these results, aiming to optimize the processes and extend the range of quantum materials that can be used, ensuring that quantum optoelectronic devices are designed around their functional requirements rather than being limited by the tools available.

References

1. Kong, Y. L. *et al.* 3D printed quantum dot light-emitting diodes. *Nano Letters* **14**, 7017–7023 (2014).
2. Yang, J. *et al.* Toward Full-Color Electroluminescent Quantum Dot Displays. *Nano Letters* **21**, 26–33 (2021).
3. Oertel, D. C., Bawendi, M. G., Arango, A. C. & Bulović, V. Photodetectors based on treated CdSe quantum-dot films. *Applied Physics Letters* **87**, 213505 (2005).
4. Clifford, J. P. *et al.* Fast, sensitive and spectrally tuneable colloidal-quantum-dot photodetectors. *Nature Nanotech* **4**, 40–44 (2009).
5. Tang, X., Ackerman, M. M., Chen, M. & Guyot-Sionnest, P. Dual-band infrared imaging using stacked colloidal quantum dot photodiodes. *Nat. Photonics* **13**, 277–282 (2019).
6. McDonald, S. A. *et al.* Solution-processed PbS quantum dot infrared photodetectors and photovoltaics. *Nature Mater* **4**, 138–142 (2005).
7. Crisp, R. W. *et al.* Metal Halide Solid-State Surface Treatment for High Efficiency PbS and PbSe QD Solar Cells. *Sci Rep* **5**, 9945 (2015).
8. Hao, M. *et al.* Ligand-assisted cation-exchange engineering for high-efficiency colloidal Cs1−xFAxPbI3 quantum dot solar cells with reduced phase segregation. *Nat Energy* **5**, 79–88 (2020).
9. Slussarenko, S. & Pryde, G. J. Photonic quantum information processing: A concise review. *Applied Physics Reviews* **6**, 041303 (2019).
10. Duan, L.-M. & Kimble, H. J. Scalable Photonic Quantum Computation through Cavity-Assisted Interactions. *Phys. Rev. Lett.* **92**, 127902 (2004).

11. Madsen, L. S. *et al.* Quantum computational advantage with a programmable photonic processor. *Nature* **606**, 75–81 (2022).

12. Tanzilli, S. *et al.* A photonic quantum information interface. *Nature* **437**, 116–120 (2005).

13. Wang, J., Sciarrino, F., Laing, A. & Thompson, M. G. Integrated photonic quantum technologies. *Nat. Photonics* **14**, 273–284 (2020).

14. Paraïso, T. K. *et al.* A photonic integrated quantum secure communication system. *Nat. Photon.* **15**, 850–856 (2021).

15. Pirandola, S., Bardhan, B. R., Gehring, T., Weedbrook, C. & Lloyd, S. Advances in photonic quantum sensing. *Nature Photon* **12**, 724–733 (2018).

16. Chang, J., Gao, J., Zadeh, I. E., Elshaari, A. W. & Zwiller, V. Nanowire-based integrated photonics for quantum information and quantum sensing. *Nanophotonics* **12**, 339–358 (2023).

17. Andersen, K. E., Fong, C. Y. & Pickett, W. E. Quantum confinement in CdSe nanocrystallites. *Journal of Non-Crystalline Solids* **299–302**, 1105–1110 (2002).

18. Brown, A. A. M. *et al.* Lead Halide Perovskite Nanocrystals: Room Temperature Syntheses toward Commercial Viability. *Advanced Energy Materials* **10**, 2001349 (2020).

19. Kairdolf, B. A., Smith, A. M. & Nie, S. One-Pot Synthesis, Encapsulation, and Solubilization of Size-Tuned Quantum Dots with Amphiphilic Multidentate Ligands. *J. Am. Chem. Soc.* **130**, 12866–12867 (2008).

20. Utzat, H. *et al.* Coherent single-photon emission from colloidal lead halide perovskite quantum dots. *Science* **363**, (2019).

21. Nguyen, H. A. *et al.* Design Rules for Obtaining Narrow Luminescence from Semiconductors Made in Solution. *Chem. Rev.* **123**, 7890–7952 (2023).

22. Westmoreland, D. E. *et al.* Properties of quantum dots coupled to plasmons and optical cavities. *The Journal of Chemical Physics* **151**, 210901 (2019).

23. Li, X., Kundaliya, D., Tan, Z. J., Anc, M. & Fang, N. X. Projection lithography patterned high-resolution quantum dots/thiol-ene photo-polymer pixels for color down conversion. *Opt. Express, OE* **27**, 30864–30874 (2019).

24. Norman, J. C., Jung, D., Wan, Y. & Bowers, J. E. Perspective: The future of quantum dot photonic integrated circuits. *APL Photonics* **3**, 030901 (2018).

25. Mullen, E. & Morris, M. A. Green Nanofabrication Opportunities in the Semiconductor Industry: A Life Cycle Perspective. *Nanomaterials* **11**, 1085 (2021).

26. Yang, Z., Pelton, M., Fedin, I., Talapin, D. V. & Waks, E. A room temperature continuous-wave nanolaser using colloidal quantum wells. *Nat Commun* **8**, 143 (2017).

27. Hoang, T. B., Akselrod, G. M. & Mikkelsen, M. H. Ultrafast Room-Temperature Single Photon Emission from Quantum Dots Coupled to Plasmonic Nanocavities. *Nano Letters* **16**, 270–275 (2016).

28. Lan, H. & Ding, Y. Ordering, positioning and uniformity of quantum dot arrays. *Nano Today* **7**, 94–123 (2012).

29. Chen, Y. *et al.* Deterministic Positioning of Colloidal Quantum Dots on Silicon Nitride Nanobeam Cavities. *Nano Lett.* **18**, 6404–6410 (2018).

30. Nguyen, H. A. *et al.* Deterministic Quantum Light Arrays from Giant Silica-Shelled Quantum Dots. *ACS Appl. Mater. Interfaces* **15**, 4294–4302 (2023).

31. Liu, Y. *et al.* Efficient All-Solution Processed Quantum Dot Light Emitting Diodes Based on Inkjet Printing Technique. *ACS Appl. Mater. Interfaces* **9**, 25506–25512 (2017).

32. Yang, P., Zhang, L., Kang, D. J., Strahl, R. & Kraus, T. High-Resolution Inkjet Printing of Quantum Dot Light-Emitting Microdiode Arrays. *Advanced Optical Materials* **8**, 1901429 (2020).

33. Jiang, C. *et al.* Coffee-Ring-Free Quantum Dot Thin Film Using Inkjet Printing from a Mixed-Solvent System on Modified ZnO Transport Layer for Light-Emitting Devices. *ACS Applied Materials and Interfaces* **8**, 26162–26168 (2016).

34. Antolini, F. & Orazi, L. Quantum Dots Synthesis Through Direct Laser Patterning: A Review. *Front. Chem.* **7**, (2019).

35. Zhan, W. *et al.* In Situ Patterning Perovskite Quantum Dots by Direct Laser Writing Fabrication. *ACS Photonics* **8**, 765–770 (2021).

36. Liang, S.-Y., Liu, Y.-F., Ji, Z.-K., Xia, H. & Sun, H.-B. Chameleon-inspired design of dynamic patterns based on femtosecond laser-induced forward transfer. *Chemical Engineering Journal* **466**, 143121 (2023).

37. Mkhize, N. & Bhaskaran, H. Electrohydrodynamic Jet Printing: Introductory Concepts and Considerations. *Small Science* **2**, 2100073 (2022).

38. Han, Y. & Dong, J. Electrohydrodynamic printing for advanced micro/nanomanufacturing: Current progresses, opportunities, and challenges. *Journal of Micro and Nano-Manufacturing* **6**, (2018).

39. Galliker, P. *et al.* Direct printing of nanostructures by electrostatic autofocussing of ink nanodroplets. *Nat. Commun.* **3**, 890 (2012).

40. Kang, G. *et al.* Electrohydrodynamic Jet-Printed MAPbBr3 Perovskite/Polyacrylonitrile Nanostructures for Water-Stable, Flexible, and Transparent Displays. *ACS Applied Nano Materials* **5**, 6726–6735 (2022).

41. Khan, M., Babinec, T., McCutcheon, M. W., Deotare, P. & Lončar, M. Fabrication and characterization of high-quality-factor silicon nitride nanobeam cavities. *Opt. Lett.* **36**, 421 (2011).

42. Jastrzebska-Perfect, P. *et al.* On-site growth of perovskite nanocrystal arrays for integrated nanodevices. *Nat Commun* **14**, 3883 (2023).

43. Hong, P.-Y. *et al.* The amazing world of self-organized Ge quantum dots for Si photonics on SiN platforms. *Appl. Phys. A* **129**, 126 (2023).

44. B. Greytak, A. *et al.* Alternating layer addition approach to CdSe/CdS core/shell quantum dots with near-unity quantum yield and high on-time fractions. *Chemical Science* **3**, 2028–2034 (2012).

45. Hanifi, D. A. *et al.* Redefining near-unity luminescence in quantum dots with photothermal threshold quantum yield. *Science* **363**, 1199–1202 (2019).

46. Proppe, A. H. *et al.* Highly stable and pure single-photon emission with 250 ps optical coherence times in InP colloidal quantum dots. *Nat. Nanotechnol.* 1–7 (2023) doi:10.1038/s41565-023-01432-0.

47. Protesescu, L. *et al.* Nanocrystals of Cesium Lead Halide Perovskites (CsPbX3, X = Cl, Br, and I): Novel Optoelectronic Materials Showing Bright Emission with Wide Color Gamut. *Nano Letters* **15**, 3692–3696 (2015).

48. Gupta, S. & Waks, E. Spontaneous emission enhancement and saturable absorption of colloidal quantum dots coupled to photonic crystal cavity. *Opt. Express, OE* **21**, 29612–29619 (2013).

49. Bauters, J. F. *et al.* Planar waveguides with less than 0.1 dB/m propagation loss fabricated with wafer bonding. *Opt. Express, OE* **19**, 24090–24101 (2011).

50. Hosseini, E. S., Yegnanarayanan, S., Atabaki, A. H., Soltani, M. & Adibi, A. High Quality Planar Silicon Nitride Microdisk Resonators for Integrated Photonics in the VisibleWavelength Range. *Opt. Express, OE* **17**, 14543–14551 (2009).

51. Brunner, H. J. C. *et al.* Fully Additive Electrohydrodynamic Inkjet-Printed TiO2 Mid-Infrared Meta-Optics. *Advanced Materials Interfaces* **9**, 2200149 (2022).

52. Derby, B. Inkjet Printing of Functional and Structural Materials: Fluid Property Requirements, Feature Stability, and Resolution. *Annual Review of Materials Research* **40**, 395–414 (2010).

53. Huang, Y. *et al.* Accurate generation of attolitre droplets for directly printing gold nanoparticles from solution through confined reaction. *Nano Ex.* **1**, 030008 (2020).

54. Schneider, J. *et al.* SI: Site-specific deposition of single gold nanoparticles by individual growth in electrohydrodynamically-printed attoliter droplet reactors. *Nanoscale* **7**, 9510–9519 (2015).

55. Rohner, P. *et al.* 3D electrohydrodynamic printing and characterisation of highly conductive gold nanowalls. *Nanoscale* **12**, 20158–20164 (2020).

56. Schirmer, N. C., Schwamb, T., Burg, B. R., Hotz, N. & Poulikakos, D. Controlled free-form fabrication of nanowires by dielectrophoretic dispension of colloids. *Applied Physics Letters* **95**, 033111 (2009).

57. Rahman, K., Khan, A., Muhammad, N. M., Jo, J. & Choi, K.-H. Fine-resolution patterning of copper nanoparticles through electrohydrodynamic jet printing. *J. Micromech. Microeng.* **22**, 065012 (2012).

58. Ren, P. & Dong, J. Direct Fabrication of VIA Interconnects by Electrohydrodynamic Printing for Multi-Layer 3D Flexible and Stretchable Electronics. *Advanced Materials Technologies* **6**, 2100280 (2021).

59. Nothnagle, C. *et al.* EHD printing of PEDOT: PSS inks for fabricating pressure and strain sensor arrays on flexible substrates. in *Next-Generation Robotics II; and Machine Intelligence and Bio-inspired Computation: Theory and Applications IX* vol. 9494 949403 (SPIE, 2015).

60. Han, Y. & Dong, J. Electrohydrodynamic (EHD) Printing of Molten Metal Ink for Flexible and Stretchable Conductor with Self-Healing Capability. *Advanced Materials Technologies* **3**, 1700268 (2018).

61. Wang, Q. *et al.* High-Resolution, Flexible, and Full-Color Perovskite Image Photodetector via Electrohydrodynamic Printing of Ionic-Liquid-Based Ink. *Advanced Functional Materials* **31**, 2100857 (2021).

62. Alzakia, F. I., Jonhson, W., Ding, J. & Tan, S. C. Ultrafast Exfoliation of 2D Materials by Solvent Activation and One-Step Fabrication of All-2D-Material Photodetectors by Electrohydrodynamic Printing. *ACS Appl. Mater. Interfaces* **12**, 28840–28851 (2020).

63. Wang, Q., Zhang, G., Zhang, H., Duan, Y. & Huang, Y. A. Electrohydrodynamically Printed Multicolor Perovskite Image Sensor Array. in *Proceedings of the 16th Annual IEEE International Conference on Nano/Micro Engineered and Molecular Systems, NEMS 2021* 652–655 (IEEE, Xiamen, China, 2021). doi:10.1109/NEMS51815.2021.9451509.

64. Jeong, J.-A., Kim, H.-K. & Kim, J. Invisible Ag grid embedded with ITO nanoparticle layer as a transparent hybrid electrode. *Solar Energy Materials and Solar Cells* **125**, 113–119 (2014).

65. Jang, Y. *et al.* Non-contact printing of high aspect ratio Ag electrodes for polycrystalline silicone solar cell with electrohydrodynamic jet printing. *Applied Physics Letters* **102**, 123901 (2013).

66. Shin, D.-Y., Seo, J.-Y., Tak, H. & Byun, D. Bimodally dispersed silver paste for the metallization of a crystalline silicon solar cell using electrohydrodynamic jet printing. *Solar Energy Materials and Solar Cells* **136**, 148–156 (2015).

67. Wu, Y. *et al.* THz Broadband Absorber Fabricated by EHD Printing Technology With High Error Tolerance. *IEEE Transactions on Terahertz Science and Technology* **9**, 637–642 (2019).

68. Kim, B. H. *et al.* High-resolution patterns of quantum dots formed by electrohydrodynamic jet printing for light-emitting diodes. *Nano Lett.* **15**, 969–973 (2015).

69. Li, H. *et al.* High-Resolution Pixelated Light Emitting Diodes Based on Electrohydrodynamic Printing and Coffee-Ring-Free Quantum Dot Film. *Advanced Materials Technologies* **5**, 2000401 (2020).

70. Wang, H. *et al.* High-efficiency and high-resolution patterned quantum dot light emitting diodes by electrohydrodynamic printing. *Nanoscale Advances* **5**, 1183–1189 (2023).

71. Kress, S. J. P. *et al.* Near-field light design with colloidal quantum dots for photonics and plasmonics. *Nano Letters* **14**, 5827–5833 (2014).

72. Kress, S. J. P. *et al.* Wedge Waveguides and Resonators for Quantum Plasmonics. *Nano Letters* **15**, 6267–6275 (2015).

73. Cohen, T. A. *et al.* Direct Patterning of Perovskite Nanocrystals on Nanophotonic Cavities with Electrohydrodynamic Inkjet Printing. *Nano Lett.* **22**, 5681–5688 (2022).

74. Vlaskin, V. A., Barrows, C. J., Erickson, C. S. & Gamelin, D. R. Nanocrystal Diffusion Doping. *J. Am. Chem. Soc.* **135**, 14380–14389 (2013).

75. Marmur, A. The Lotus Effect: Superhydrophobicity and Metastability. *Langmuir* **20**, 3517–3519 (2004).

76. Geiregat, P., Allan, G., Hens, Z. & Delerue, C. Single-exciton optical gain in semiconductor nanocrystals: Positive role of electron-phonon coupling. *Phys. Rev. B* **93**, 115416 (2016).

77. Huang, C.-Y. *et al.* CsPbBr3 Perovskite Quantum Dot Vertical Cavity Lasers with Low Threshold and High Stability. *ACS Photonics* **4**, 2281–2289 (2017).

78. Lim, J., Park, Y.-S. & Klimov, V. I. Optical gain in colloidal quantum dots achieved with direct-current electrical pumping. *Nat Mater* **17**, 42–49 (2018).

79. Jung, H., Ahn, N. & Klimov, V. I. Prospects and challenges of colloidal quantum dot laser diodes. *Nat. Photon.* **15**, 643–655 (2021).

80. Walsh, K. M., Pressler, K., Crane, M. J. & Gamelin, D. R. Ferromagnetism and Spin-Polarized Luminescence in Lead-Free CsEuCl3 Perovskite Nanocrystals and Thin Films. *ACS Nano* **16**, 2569–2576 (2022).

81. De Siena, M. C. *et al.* Two-Dimensional van der Waals Nanoplatelets with Robust Ferromagnetism. *Nano Lett.* **20**, 2100–2106 (2020).

82. Pressler, K., Snoeren, T. J., Walsh, K. M. & Gamelin, D. R. Magnetic Amplification at Yb^{3+} "Designer Defects" in the van der Waals Ferromagnet CrI_3. *Nano Lett.* **23**, 1320–1326 (2023).

83. Milstein, T. J., Kroupa, D. M. & Gamelin, D. R. Picosecond Quantum Cutting Generates Photoluminescence Quantum Yields over 100% in Ytterbium-Doped CsPbCl3 Nanocrystals. *Nano Letters* **18**, 3792–3799 (2018).

84. Pernice, W. H. P., Xiong, C., Schuck, C. & Tang, H. X. High-Q aluminum nitride photonic crystal nanobeam cavities. *Applied Physics Letters* **100**, 091105 (2012).

85. Frank, I. W., Lončar, M., McCutcheon, M. W. & Deotare, P. B. Programmable photonic crystal nanobeam cavities. *Optics Express* **18**, 8705–8712 (2010).

86. Hodaei, H., Miri, M.-A., Heinrich, M., Christodoulides, D. N. & Khajavikhan, M. Parity-time–symmetric microring lasers. *Science* **346**, 975–978 (2014).

87. Zhang, S., Yong, Z., Zhang, Y. & He, S. Parity-Time Symmetry Breaking in Coupled Nanobeam Cavities. *Sci Rep* **6**, 24487 (2016).

88. Wei, W.-Q. *et al.* Monolithic integration of embedded III-V lasers on SOI. *Light Sci Appl* **12**, 84 (2023).

89. Hail, C. U. *et al.* Nanoprinting organic molecules at the quantum level. *Nature Communications* **10**, 1–8 (2019).

90. Manna, A. *et al.* Cryo-Compatible In Situ Strain Tuning of 2D Material-Integrated Nanocavity. *ACS Photonics* **10**, 3242–3247 (2023).

91. Barelli, M. *et al.* Single-Photon Emitting Arrays by Capillary Assembly of Colloidal Semiconductor CdSe/CdS/SiO2 Nanocrystals. *ACS Photonics* **10**, 1662–1670 (2023).

92. Tilford, T. *et al.* Comparative Reliability of Inkjet-Printed Electronics Packaging. *IEEE Trans. Compon. Packag. Manuf. Technol.* **11**, 351–362 (2021).

93. Liu, Y. *et al.* Inkjet Printed Metal–Organic Frameworks for Non-Volatile Memory Devices Suitable for Printed RRAM. *Adv. Funct. Mater.* **n/a**, 2412372.

94. Kunnari, E., Valkama, J., Keskinen, M. & Mansikkamäki, P. Environmental evaluation of new technology: printed electronics case study. *Journal of Cleaner Production* **17**, 791–799 (2009).

95. Zheng, L.-R., Tenhunen, H. & Zou, Z. Life Cycle Assessment (LCA) for Printed Electronics. in *Smart Electronic Systems* 243–267 (John Wiley & Sons, Ltd, 2018). doi:10.1002/9783527691685.ch10.

96. Fujii, M. Evolution Theory of Ink Jet Technologies: Progress by Component or Architectural Knowledge. *JIST* **62**, 040502-1-040502–7 (2018).

97. Park, J. U. *et al.* High-resolution electrohydrodynamic jet printing. *Nat. Mater.* **6**, 782–789 (2007).

98. Niklas Schirmer, B. C. *et al.* On Ejecting Colloids Against Capillarity from Sub-micrometer Openings: On-Demand Dielectrophoretic Nanoprinting. *Adv. Mater.* **22**, 4701–4705 (2010).

99. Richner, P. *et al.* Printable Nanoscopic Metamaterial Absorbers and Images with Diffraction-Limited Resolution. *ACS Appl. Mater. Interfaces* **8**, 11690–11697 (2016).

100. Zhang, B. *et al.* One-Step Sub-micrometer-Scale Electrohydrodynamic Inkjet Three-Dimensional Printing Technique with Spontaneous Nanoscale Joule Heating. *ACS Appl. Mater. Interfaces* **9**, 29965–29972 (2017).

101. Lee, J.-S. *et al.* Design and evaluation of a silicon based multi-nozzle for addressable jetting using a controlled flow rate in electrohydrodynamic jet printing. *Appl. Phys. Lett.* **93**, 243114 (2008).

102. Khan, A. *et al.* Fabrication of circuits by multi-nozzle electrohydrodynamic inkjet printing for soft wearable electronics. *JMR* **36**, 3568–3578 (2021).

103. Guymon, G. G. *et al.* Electrohydrodynamic Printing-Based Heterointegration of Quantum Dots on Suspended Nanophotonic Cavities. *Adv. Mater. Technol.* **9**, 2301921 (2024).

104. Choi, J.-H. *et al.* Exploiting the colloidal nanocrystal library to construct electronic devices. *Science* **352**, 205–208 (2016).

105. Olshansky, J. H. *et al.* Using Photoexcited Core/Shell Quantum Dots To Spin Polarize Appended Radical Qubits. *J. Am. Chem. Soc.* **142**, 13590–13597 (2020).

106. Hetsch, F., Zhao, N., Kershaw, S. V. & Rogach, A. L. Quantum dot field effect transistors. *Mater. Today* **16**, 312–325 (2013).

107. Shibata, K. *et al.* Single PbS colloidal quantum dot transistors. *Nat. Commun.* **14**, 7486 (2023).

108. Kovalenko, M. V., Protesescu, L. & Bodnarchuk, M. I. Properties and potential optoelectronic applications of lead halide perovskite nanocrystals. *Science* **358**, 745–750 (2017).

109. Shamsi, J., Rainò, G., Kovalenko, M. V. & Stranks, S. D. To nano or not to nano for bright halide perovskite emitters. *Nat. Nanotechnol.* **16**, 1164–1168 (2021).

110. Kagan, C. R., Bassett, L. C., Murray, C. B. & Thompson, S. M. Colloidal Quantum Dots as Platforms for Quantum Information Science. *Chem. Rev.* **121**, 3186–3233 (2021).

111. Yun, H. J. *et al.* Solution-processable integrated CMOS circuits based on colloidal CuInSe2 quantum dots. *Nat. Commun.* **11**, 5280 (2020).

112. Nguyen, H. A. *et al.* Colossal Core/Shell CdSe/CdS Quantum Dot Emitters. *ACS Nano* **18**, 20726–20739 (2024).

113. Chen, Y. *et al.* "Giant" Multishell CdSe Nanocrystal Quantum Dots with Suppressed Blinking. *J. Am. Chem. Soc.* **130**, 5026–5027 (2008).

114. Cao, W., Chern, M., Dennis, A. M. & Brown, K. A. Measuring Nanoparticle Polarizability Using Fluorescence Microscopy. *Nano Lett.* **19**, 5762–5768 (2019).

115. Klein, T. *et al.* Liquid Viscosity and Surface Tension of n-Hexane, n-Octane, n-Decane, and n-Hexadecane up to 573 K by Surface Light Scattering. *J. Chem. Eng. Data* **64**, 4116–4131 (2019).

116. Kallio, T., Laine, J. & Stenius, P. Intermolecular Interactions and the Adhesion of Oleic Acid. *J. Disper. Sci. Technol.* **30**, 222–230 (2009).

117. Green, N. G. & Nili, H. Dielectrophoresis. in *Encyclopedia of Nanotechnology* (ed. Bhushan, B.) 534–543 (Springer Netherlands, Dordrecht, 2012). doi:10.1007/978-90-481-9751-4_131.

118. Hywel, M. & Green, N. *AC Electrokinetics: Colloids and Nanoparticles*. (Research Studies Press, 2003).

119. Goyal, M. & Singh, M. Size and shape dependence of optical properties of nanostructures. *Appl. Phys. A* **126**, 176 (2020).

120. Suresh, S. & Arunseshan, C. Dielectric Properties of Cadmium Selenide (CdSe) Nanoparticles synthesized by solvothermal method. *Appl. Nanosci.* **4**, 179–184 (2014).

121. Trewby, W. & Voïtchovsky, K. Nanoscale probing of local dielectric changes at the interface between solids and aqueous saline solutions. *Faraday Discuss.* **246**, 387–406 (2023).

122. Pirolli, L., Goodwin, A. R. H., Marsh, K. N. & May, E. F. Determination of the Relative Permittivity, εr, of Octane at Temperatures between (303 and 393) K and Pressures below 25 MPa with a Concentric Cylinder Capacitor at a Frequency of 1 kHz. *J. Chem. Eng. Data* **59**, 1609–1613 (2014).

123. Moualkia, H., Hariech, S., Aida, M. S., Attaf, N. & Laifa, E. L. Growth and physical properties of CdS thin films prepared by chemical bath deposition. *J. Phys. D: Appl. Phys.* **42**, 135404 (2009).

124. Nair, P. K., nair, M. T. S., Campos, J. & Sansores, L. E. A critical discussion of the very high photoconductivity in chemically deposited cadmium sulfide thin films: Implications for solar cell technology. *Solar Cells* **22**, 211–227 (1987).

125. Martínez-Landeros, V. H., Hernandez-Como, N., Gutierrez-Heredia, G., Quevedo-Lopez, M. A. & Aguirre-Tostado, F. S. Structural, chemical and electrical properties of CdS thin films fabricated by pulsed laser deposition using varying background gas pressure. *Thin Solid Films* **682**, 24–28 (2019).

126. Lee, S. F. & Osborne, M. A. Brightening, Blinking, Bluing and Bleaching in the Life of a Quantum Dot: Friend or Foe? *ChemPhysChem* **10**, 2174–2191 (2009).

127. Onses, M. S., Sutanto, E., Ferreira, P. M., Alleyne, A. G. & Rogers, J. A. Mechanisms, Capabilities, and Applications of High-Resolution Electrohydrodynamic Jet Printing. *Small* **11**, 4237–4266 (2015).

128. Limonov, M. F., Rybin, M. V., Poddubny, A. N. & Kivshar, Y. S. Fano resonances in photonics. *Nat. Photon.* **11**, 543–554 (2017).

129. Berkinsky, D. B. *et al.* Narrow Intrinsic Line Widths and Electron–Phonon Coupling of InP Colloidal Quantum Dots. *ACS Nano* **17**, 3598–3609 (2023).

130. Cheng, L.-P. *et al.* Efficient CsPbBr3 Perovskite Light-Emitting Diodes Enabled by Synergetic Morphology Control. *Advanced Optical Materials* **7**, 1801534 (2019).

131. Yantara, N. *et al.* Inorganic Halide Perovskites for Efficient Light-Emitting Diodes. *J. Phys. Chem. Lett.* **6**, 4360–4364 (2015).

132. Cao, X. *et al.* Achieving one-step solution deposition of high quality CsPbBr3 films for efficient solar cells through halide ion exchange. *Journal of Alloys and Compounds* **919**, 165722 (2022).

133. Purkayastha, P. *et al.* Purcell Enhanced Emission and Saturable Absorption of Cavity-Coupled CsPbBr3 Quantum Dots. *ACS Photonics* **11**, 1638–1644 (2024).

134. Xu, J. *et al.* Size-tunable CsPbBr3 perovskite ring arrays for lasing. *Nanoscale* **10**, 10383–10388 (2018).

135. Vila-Liarte, D. *et al.* Templated-Assembly of CsPbBr3 Perovskite Nanocrystals into 2D Photonic Supercrystals with Amplified Spontaneous Emission. *Angewandte Chemie International Edition* **59**, 17750–17756 (2020).

136. McGrath, F., Ghorpade, U. V. & Ryan, K. M. Synthesis and dimensional control of CsPbBr3 perovskite nanocrystals using phosphorous based ligands. *The Journal of Chemical Physics* **152**, 174702 (2020).

137. Zhong, Q. *et al.* One-Pot Synthesis of Highly Stable CsPbBr3@SiO2 Core–Shell Nanoparticles. *ACS Nano* **12**, 8579–8587 (2018).

138. Gu, Z. *et al.* Direct-Writing Multifunctional Perovskite Single Crystal Arrays by Inkjet Printing. *Small* **13**, 1603217 (2017).

139. Corzo, D. *et al.* A Universal Cosolvent Evaporation Strategy Enables Direct Printing of Perovskite Single Crystals for Optoelectronic Device Applications. *Advanced Materials* **34**, 2109862 (2022).

140. Stringer, J. & Derby, B. Limits to feature size and resolution in ink jet printing. *Journal of the European Ceramic Society* **29**, 913–918 (2009).

141. Dirin, D. N., Cherniukh, I., Yakunin, S., Shynkarenko, Y. & Kovalenko, M. V. Solution-Grown CsPbBr3 Perovskite Single Crystals for Photon Detection. *Chem. Mater.* **28**, 8470–8474 (2016).

142. Shi, J. *et al.* Studies on the optical stability of CsPbBr3 with different dimensions (0D, 1D, 2D, 3D) under thermal environments. *Nanoscale* **15**, 11190–11198 (2023).

143. Zhao, J. *et al.* Great Disparity in Photoluminesence Quantum Yields of Colloidal CsPbBr3 Nanocrystals with Varied Shape: The Effect of Crystal Lattice Strain. *J. Phys. Chem. Lett.* **8**, 3115–3121 (2017).

144. Zhang, Y. *et al.* Surface Reconstruction of CsPbBr3 Nanocrystals by the Ligand Engineering Approach for Achieving High Quantum Yield and Improved Stability. *Langmuir* **39**, 6222–6230 (2023).

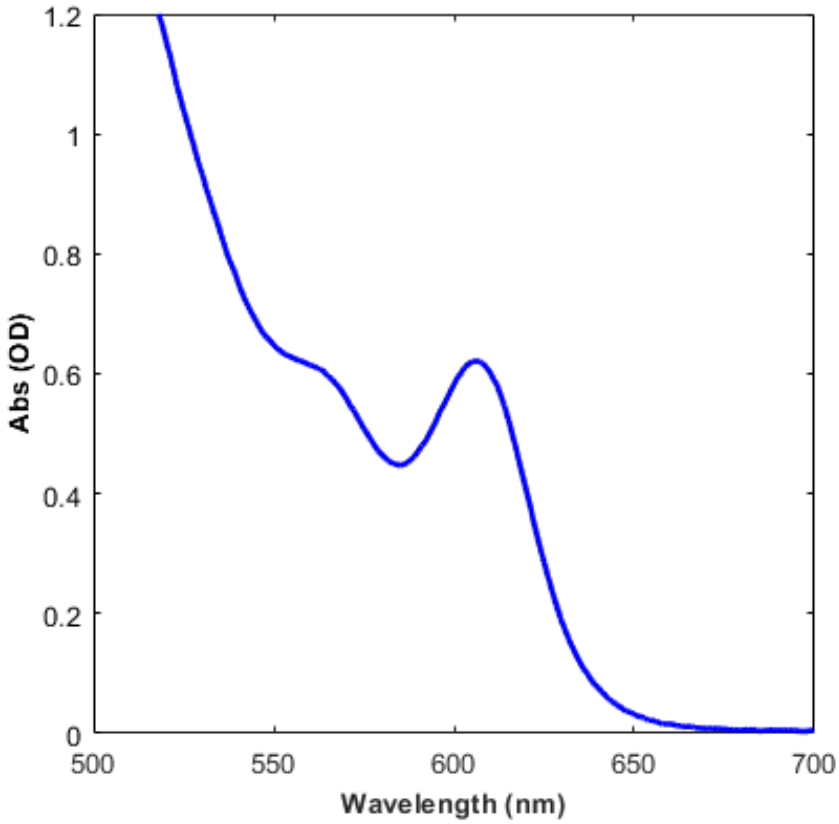

Figure A1. Absorption spectrum of the as-synthesized CdSe/CdS ink. Optical density (0.6) of the first exitonic peak indicated an almost-suitable concentration for electrohydrodynamic inkjet printing. To further increase the concentration, the QDs were crashed from solution and redispersed in 1:1 octane:hexadecane at a respective solution ratio of 4:3, to reach a target OD of 0.8.

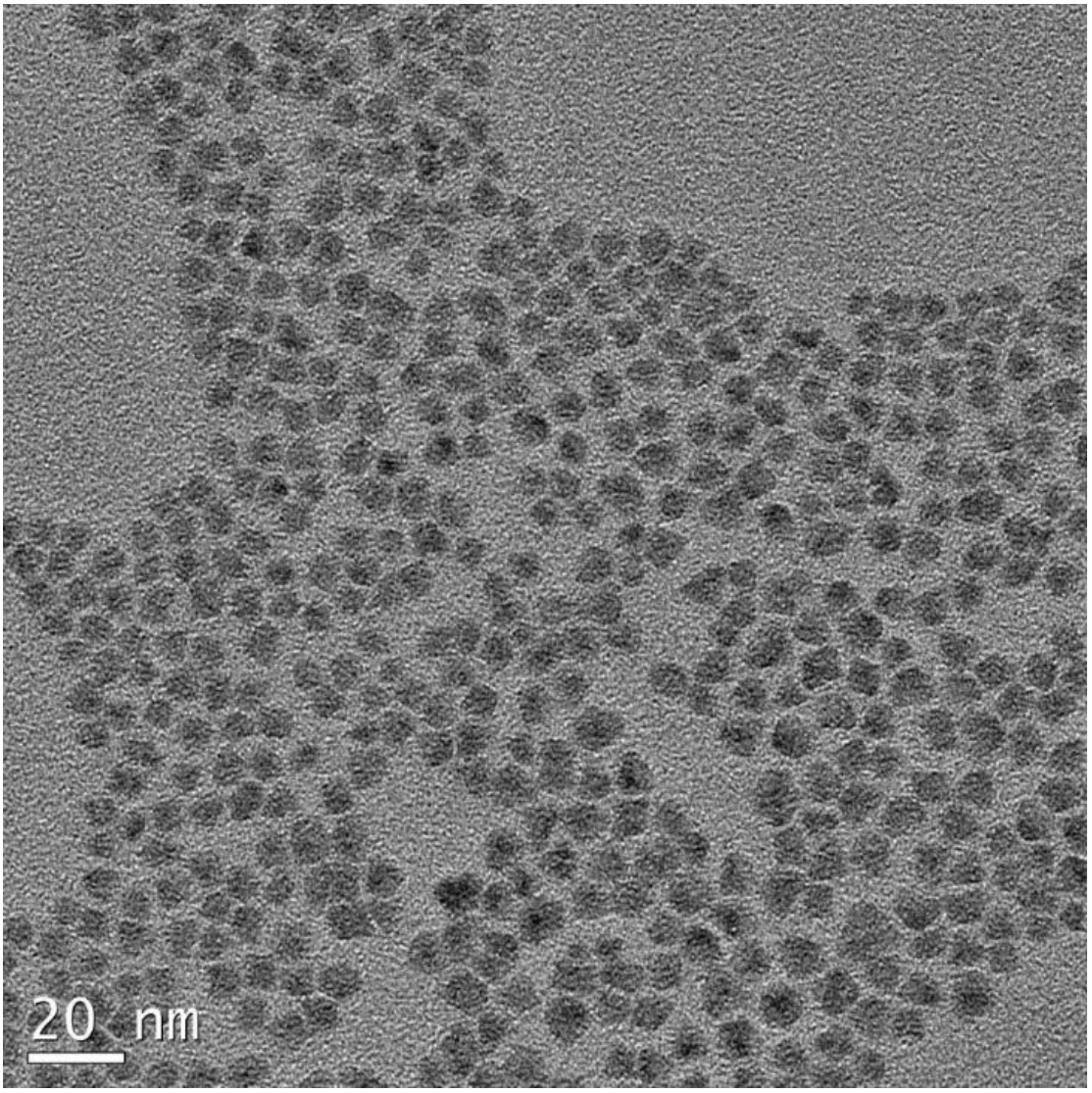

Figure A2. Transmission electron microscopy (TEM) of the CdSe/CdS quantum dots (QDs). An average cross-sectional length of $\mathbf{6.1 \pm 0.8}$ nm calculated using particle analysis software (ImageJ).

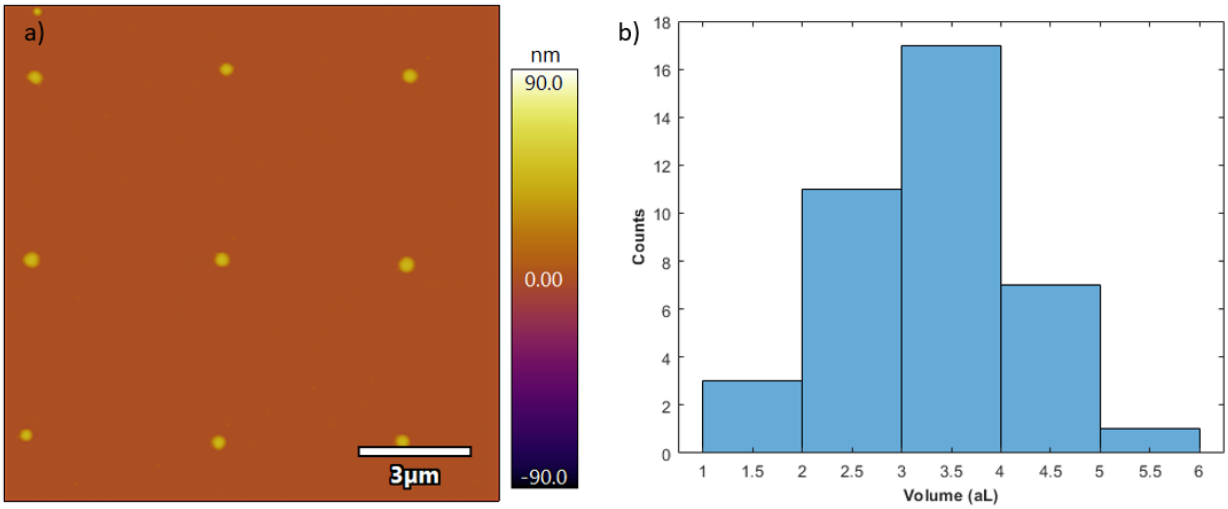

Figure A3. EHDIJ print size analysis. a) Atomic force microscopy of EHDIJ printed CdSe/CdS quantum dots. b) Histogram of the volumes of EHIDIJ printed QDs ($\boldsymbol{n = 39}$). A mean volume of $\boldsymbol{3.33 \pm 0.86}$ attoliters (aL) was calculated using particle analysis software (Asylum Research).

A1. Determination of Purcell enhancement

The maximum possible Purcell enhancement for these heterointegrated silicon nitride air-suspended nanophotonic cavities is given by,

$$F_P = 1 + \frac{3\,\lambda^3\,Q_{em}}{4\,\pi^2 n^3 V}\psi(\boldsymbol{r}) \qquad (A1)$$

Where emitter quality factor (Q_{em}) is 22, maximum E-field intensity ratio ($\psi(\boldsymbol{r})$) is 0.41, cavity's index of refraction (n) is 2 and mode volume (V) is given as,

$$V = 2\left(\frac{\lambda}{n^3}\right)^3 \qquad (A2)$$

Which results in a maximum theoretical Purcell enhancement of 1.34.

To determine the actual Purcell enhancement, photoluminescent (PL) lifetime measurements were performed with an optical testbed using a 532 nm source, at 10 MH excitation, and ~100 ps full-width half-maximum pulse width. Uncoupled quantum dot ensembles were measured, as-printed, showing mean ($N = 6$) fast and slow lifetimes of 1.18 ± 0.07 ns and 5.31 ± 0.17 ns, respectively. The mean fast and slow lifetimes of the cavity-coupled QDs, with a biexponential fit, was 1.02 ns and 4.13 ns, respectively. This corresponds to a Purcell enhancement of 1.15 and 1.29 for the fast and slow lifetimes, respectively.

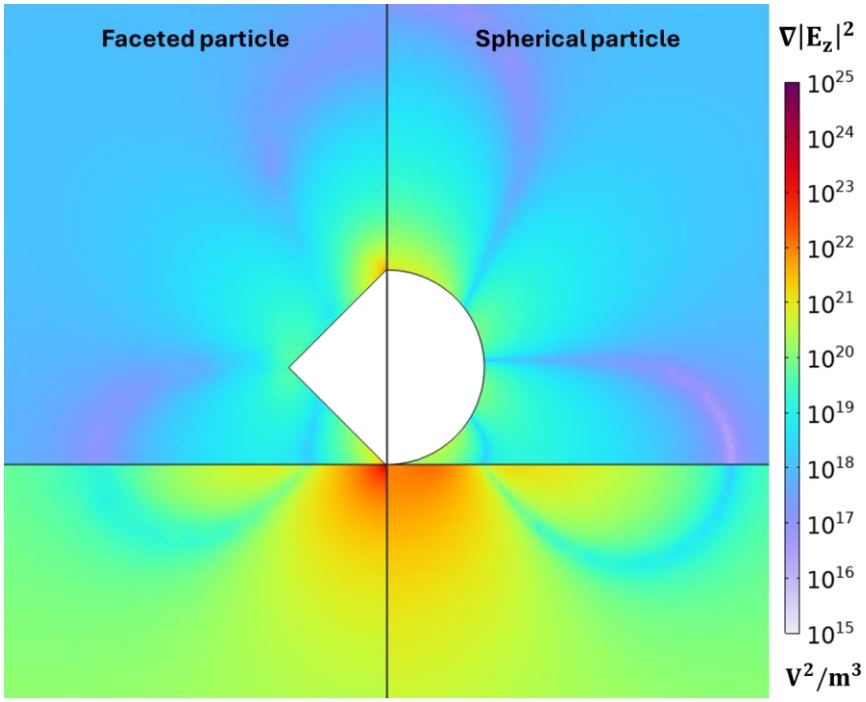

Figure A4: COMSOL simulated particle geometries. Plotted gradient of the squared magnitude of the electric field, with respect to the vertical z-axis, of a faceted and spherical particle.

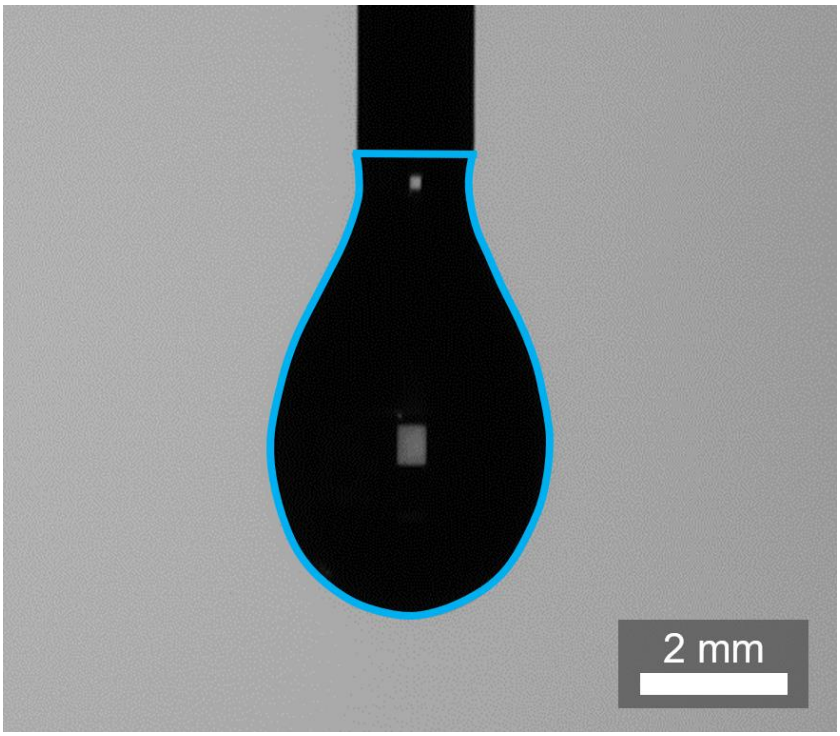

Figure A5: Pendant drop test. Shadow image of octane:hexadecane pendant drop shape analysis. Pendant drop outline (blue) indicates shape profile used for surface tension measurement.

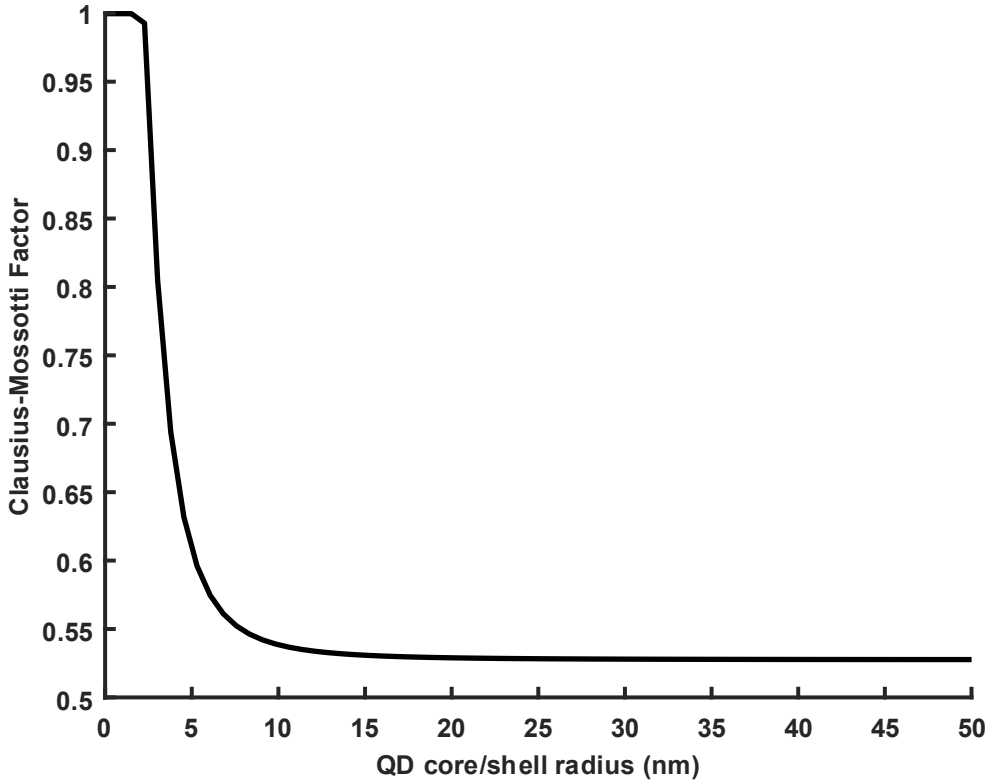

Figure A6: Clausius-Mossotti factor for core/shell QD. Plotted approximation of Clausius-Mossotti factor of a core/shell QD based on the volumetric ratio between the CdSe core and CdS shell. The permittivity values (at 1 kHz) used for the CdSe core, CdS shell, and solvent medium used were: 20,000[108], 8.7[107], and 2.0[108,109] respectively.

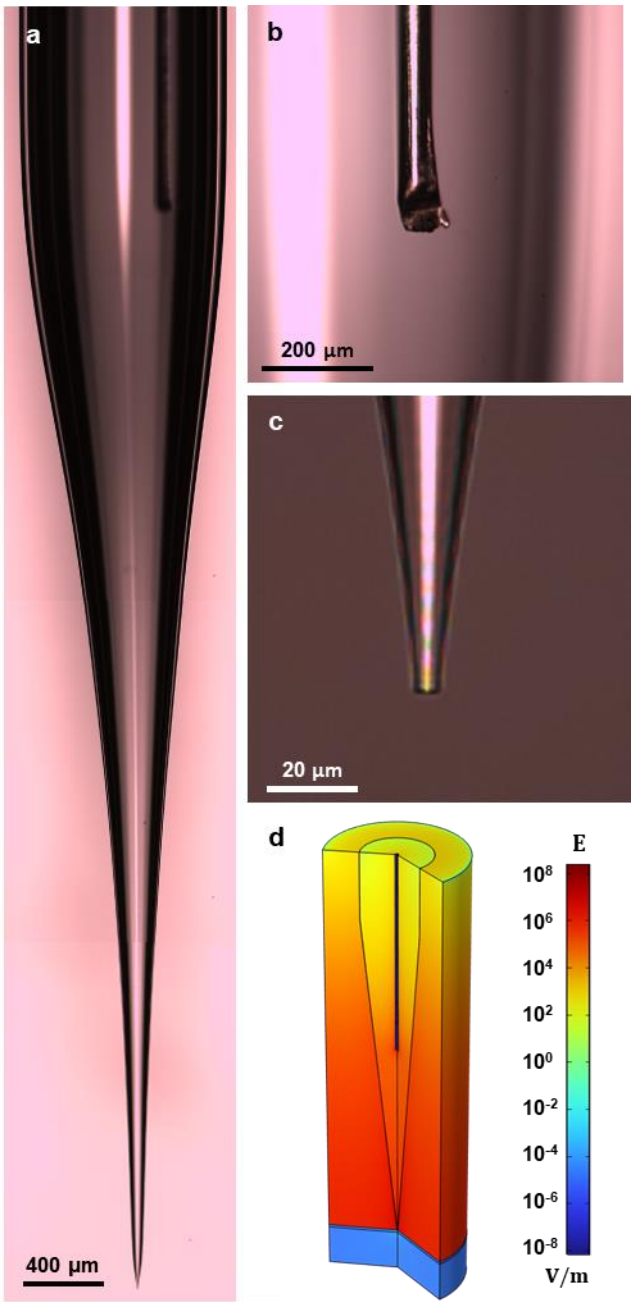

Figure A7: Printhead analysis and simulation. a, b, and c, Brightfield microscopy images of (a) EHDIJ printhead, (b) interior electrode tip, and (c) printhead tip. (d) Finite element analysis simulating electric field in/around the printhead, substrate, and ground plane.

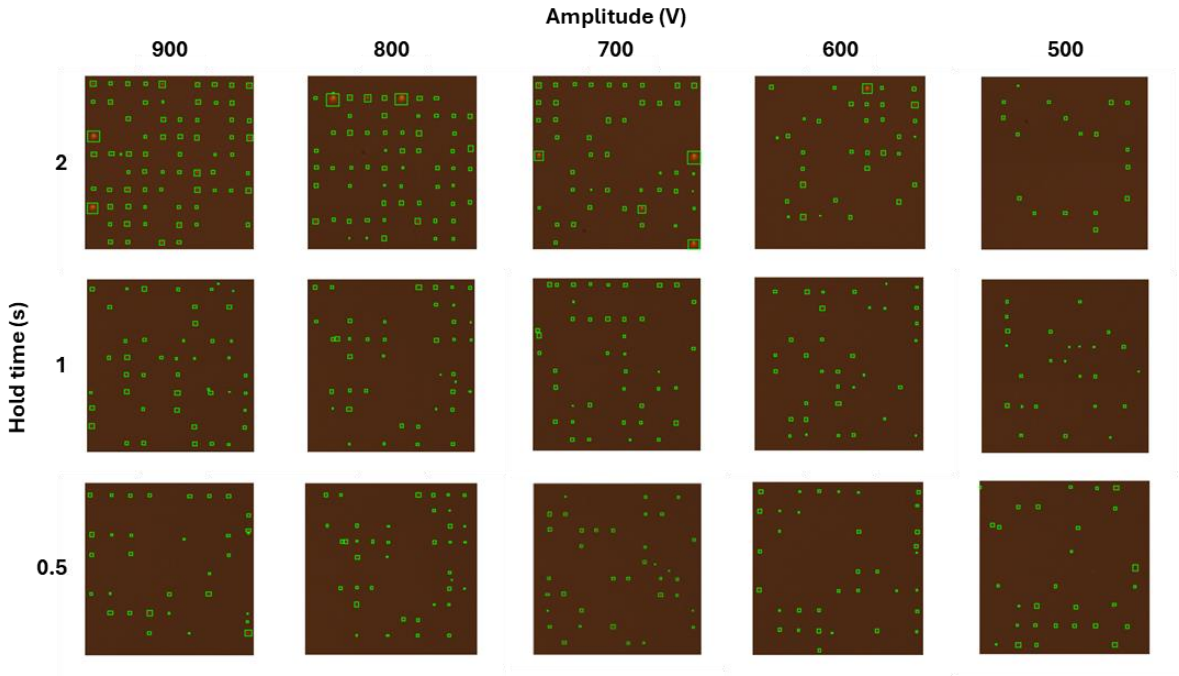

Figure A8: MATLAB machine vision for print detection. Fluorescent microscopy images of EHDIJ prints in an array of amplitudes and hold times with 5 μm print spacing. Green boxes indicate discrete prints detected by MATLAB image processing toolbox.

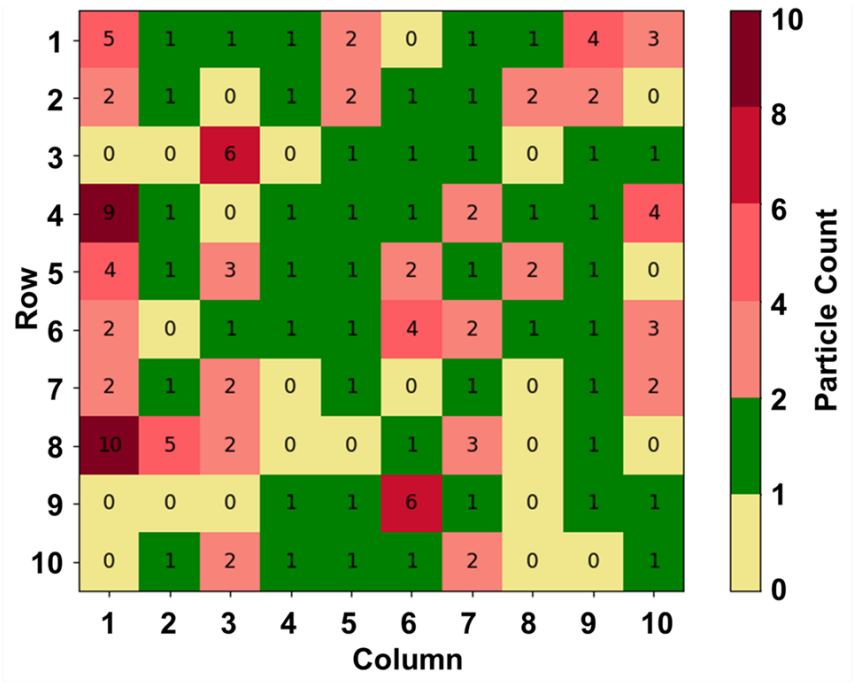

Figure A9: Heatmap of SEM analysis. Plotted heatmap summary of the number of QDs counted per print attempt site, via SEM, for the 900 V and 2 s parameter configuration. Images from each print attempt site are included in Extended Data 1.

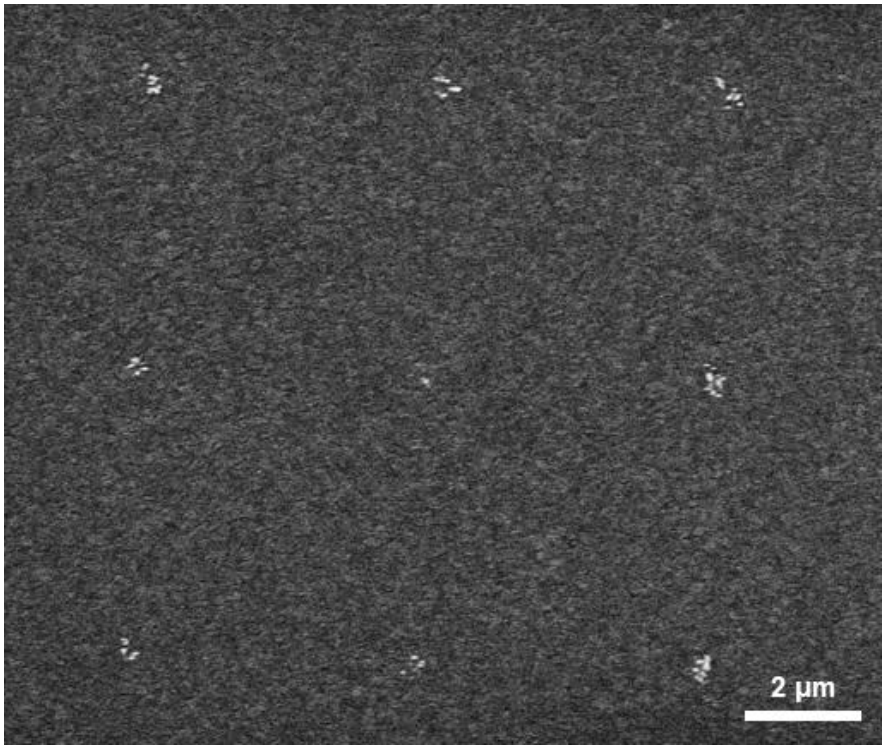

Figure A10: Smaller colossal CdSe/CdS printing results. Scanning electron microscopy of 3x3 array of printed CdSe/CdS QD ensembles. Synthesized with 30 CdS monolayers, with an average diameter of $\mathbf{26.3 \pm 2.2}$ nm.

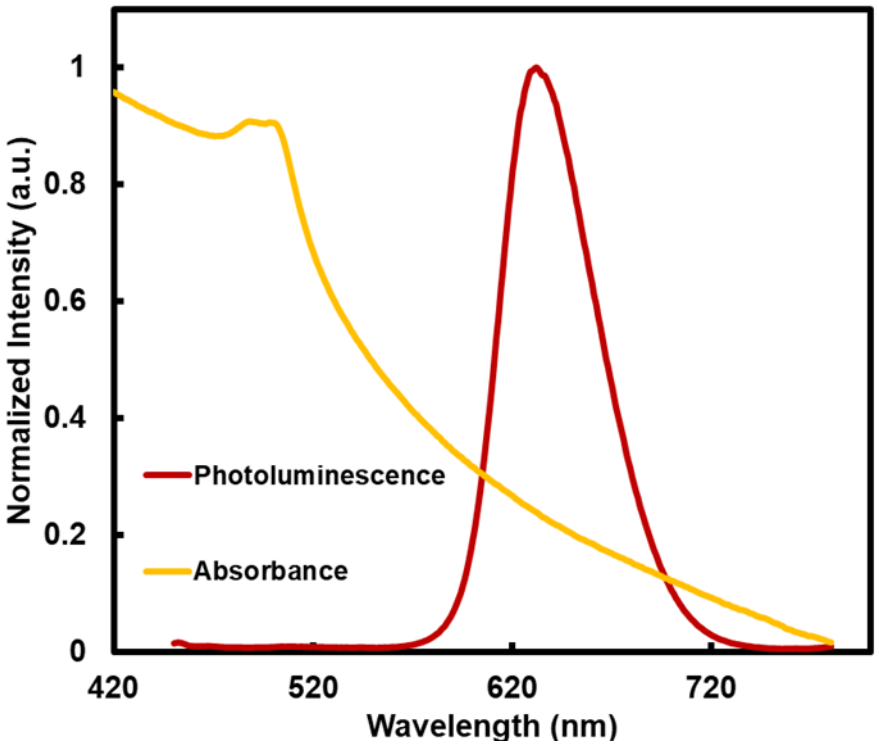

Figure A11: Colloidal QD spectral characterization. Plotted spectrum of the Photoluminescence and absorbance of 80 ML CdSe/CdS QDs, as measured in hexane.

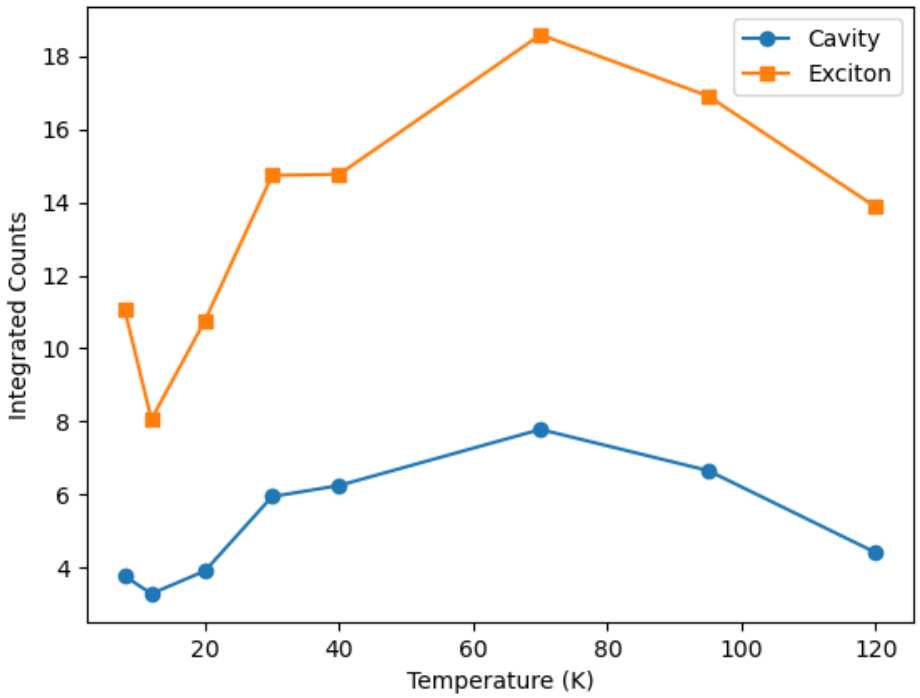

Figure A12: QD-cavity temperature sweep. Plotted integrated counts of cavity mode and excitonic emission across a range of temperatures. Highest intensity of emission measured at 70 K.

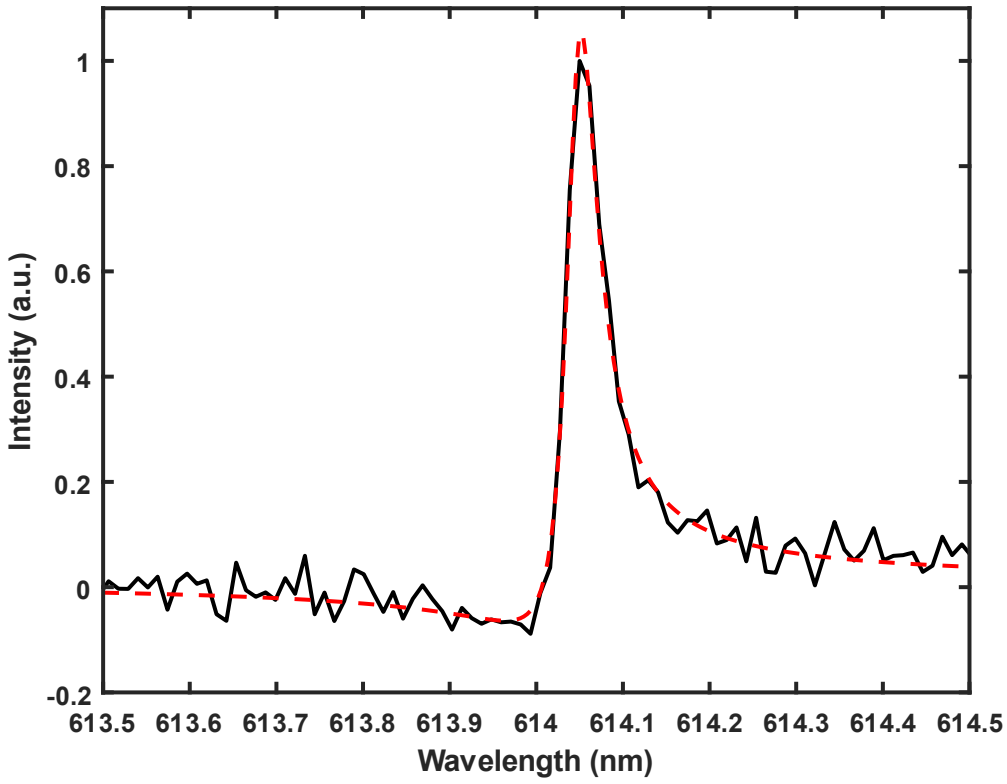

Figure A13: Spectrum of cavity mode. Plotted spectrum of QD-integrated cavity mode (black) with Fano fit (red). Measured at room temperature with 10 μW excitation.

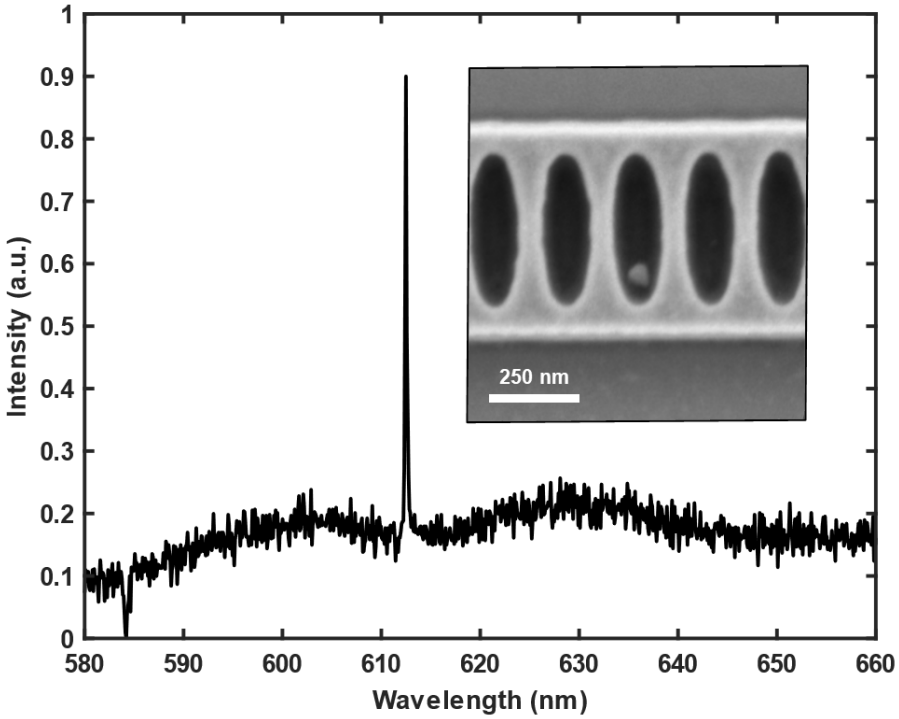

Figure A14: Photobleached heterointegrated QD-cavity. Plotted spectrum of heterointegrated QD that photobleached during spectral analysis, leaving only the SiN background and cavity mode emission. Inset: SEM image of EHD-printed QD in cavity.

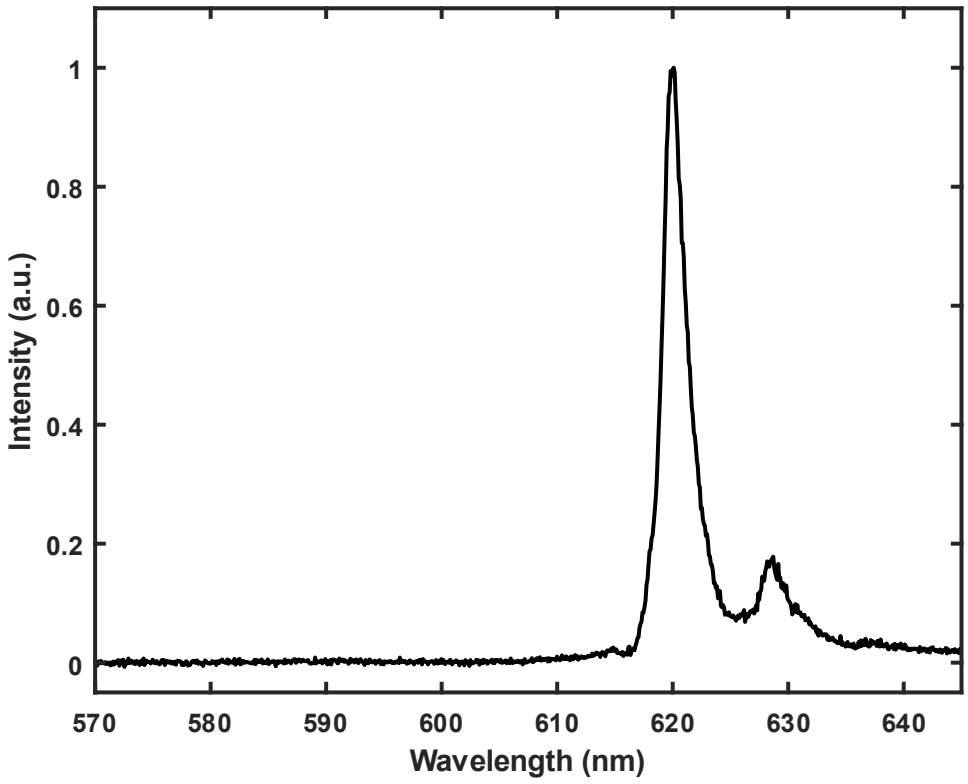

Figure A15: Spectrum of colossal CdSe/CdS QD at 8 K. Plotted spectrum of colossal CdSe/CdS QD (80 CdS monolayers) measured at 8 K and 1 μW excitation. Measured on SiO_2 substrate.

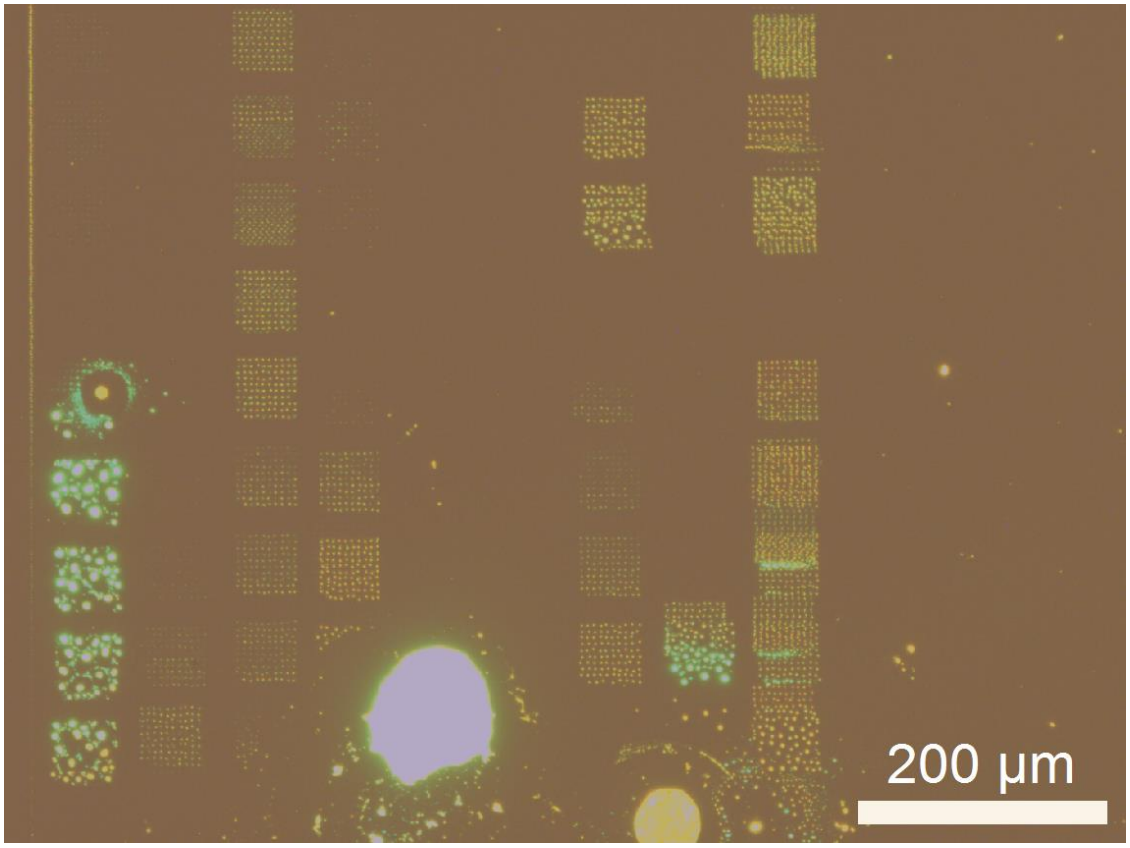

Figure A16. Fluorescent microscopy of initial perovskite printing trails with a much lower ratio of low-vapor pressure solvent (10% CHP), resulting in clogging, electrospray, and twin jetting.

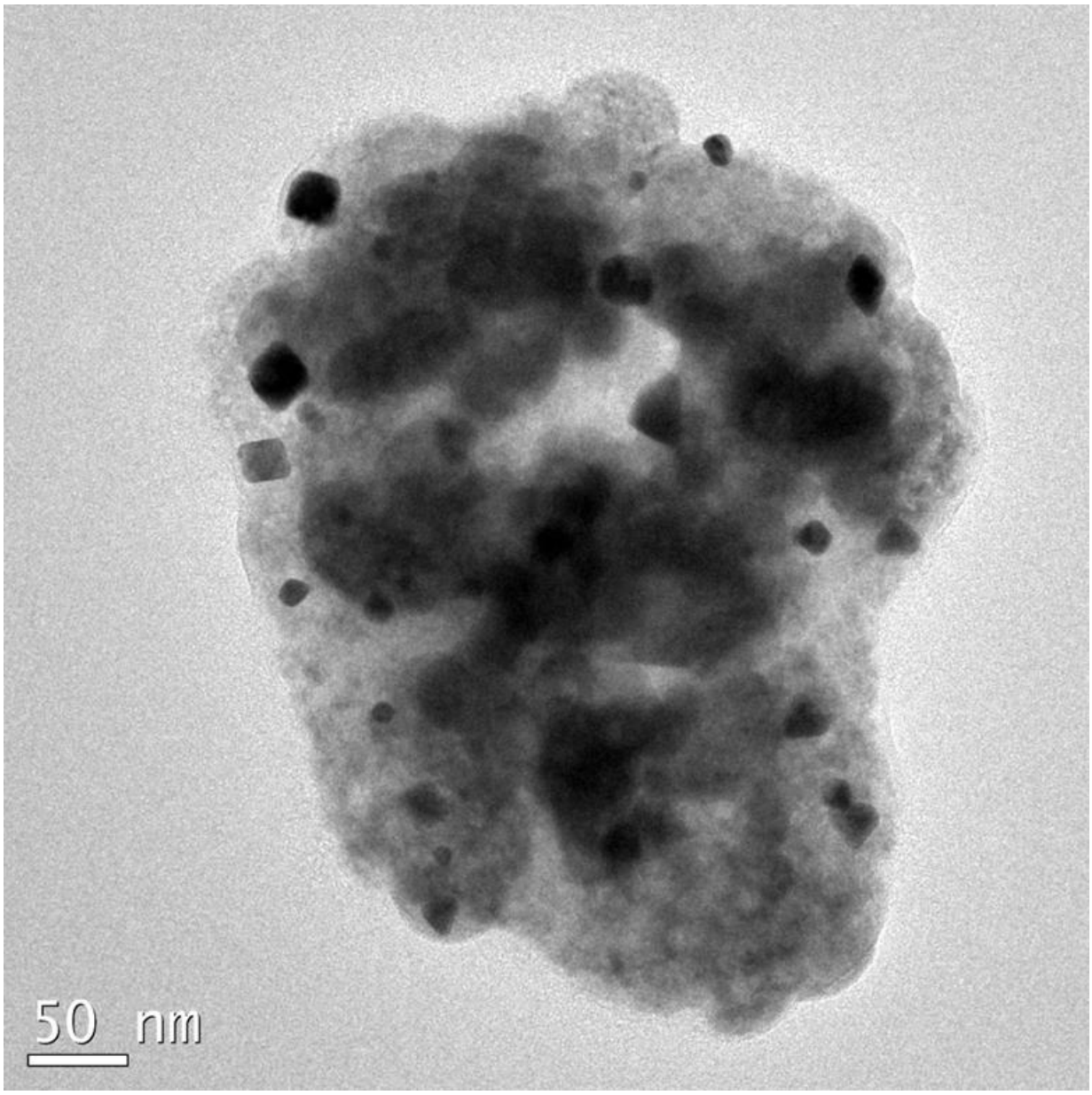

Figure A17. TEM image of 0.5 mM 1:39 DMSO:CHP $CsPbBr_3$ EHDIJ printed perovskite core formation discussed in Figure 3.2C.

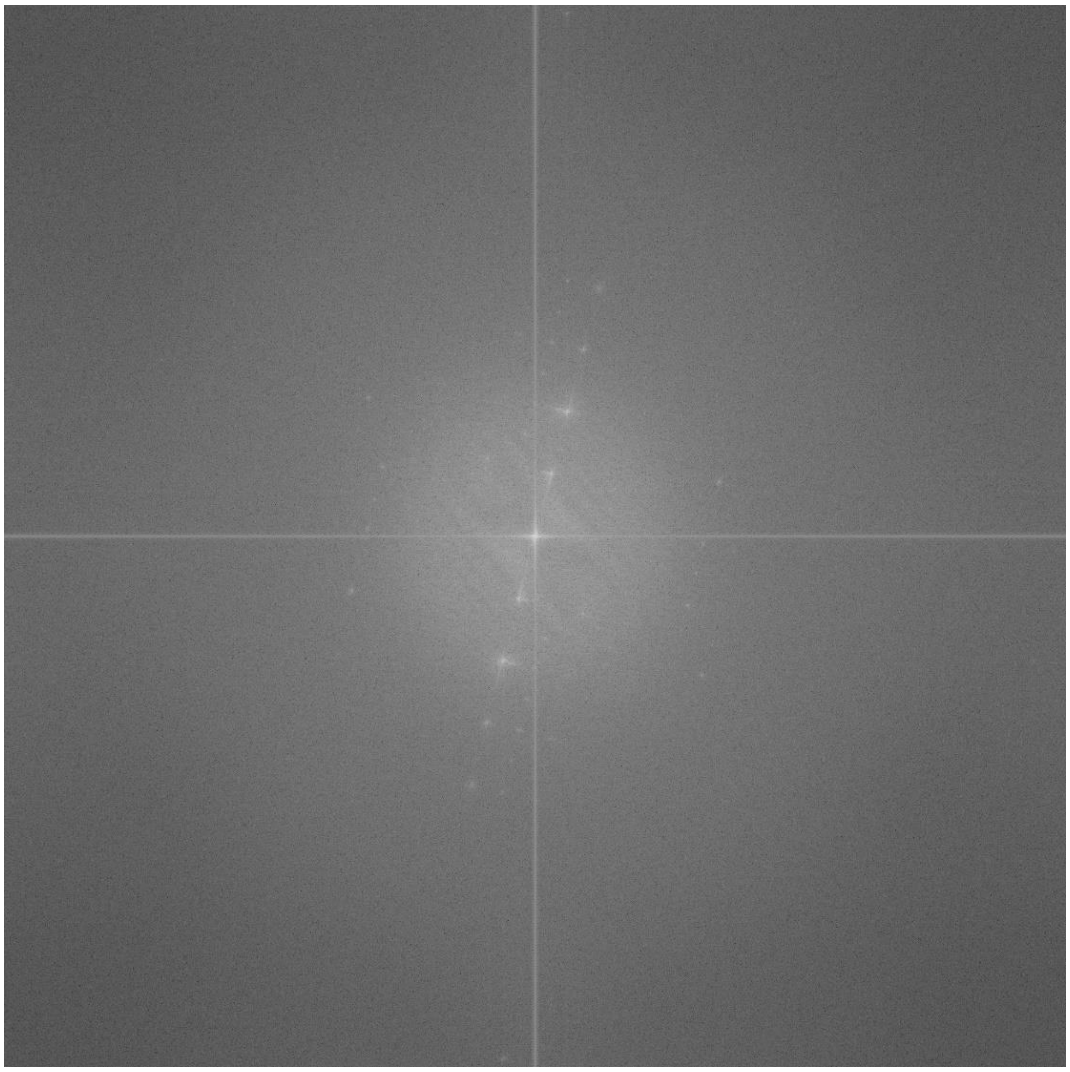

Figure A18. Electron diffraction of 0.5 mM 1:39 DMSO:CHP $CsPbBr_3$ EHDIJ printed perovskite. Analysis of diffraction pattern shows lattice d-spacings that correspond with an orthorhombic crystal phase.

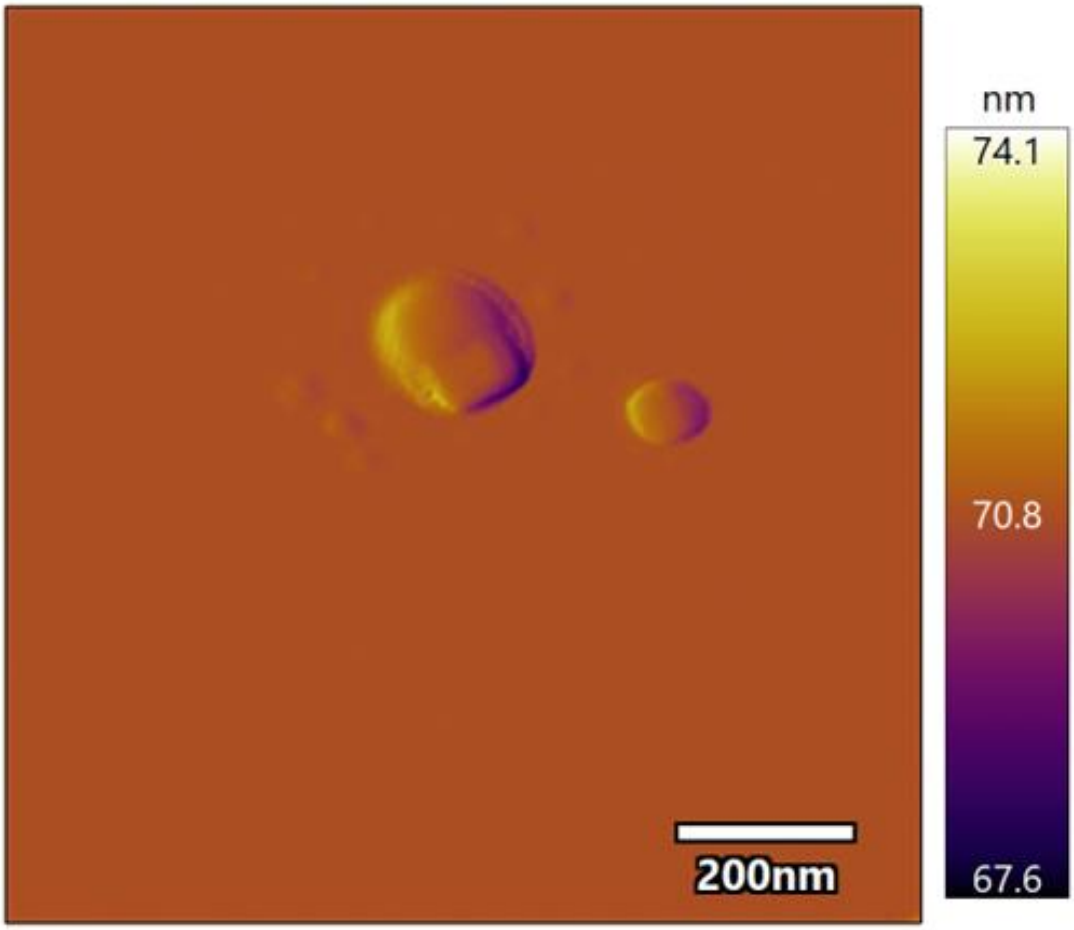

Figure A19. AFM image of 10 mM 1:39 DMSO:CHP $CsPbBr_3$ EHDIJ printed perovskite annealed under active vacuum.